remote sensing

MDPI

Article

Spatiotemporal Dynamics and Driving Mechanisms of Impervious Surface Expansion in Changsha County Using Landsat Time-Series

Yitian Cao [1,2], Lihong Zhu [1,2,*], Yiman Li [3], Qing Xia [2], Qiong Zheng [2], Zishuo Wu [2] and Xiaoyin Yang [2]

[1] Engineering Laboratory of Spatial Information Technology of Highway Geological Disaster Early Warning in Hunan Province, Changsha University of Science & Technology, Changsha 410114, China; yitian_rain@hotmail.com
[2] School of Aeronautic Engineering, Changsha University of Science & Technology, Changsha 410114, China; xiaqing@csust.edu.cn (Q.X.); zhengq@csust.edu.cn (Q.Z.); wuzishuo@csust.edu.cn (Z.W.); 202404250143@csust.edu.cn (X.Y.)
[3] School of Information Engineering, China University of Geosciences Beijing, Beijing 100083, China; 3004200003@email.cugb.edu.cn
* Correspondence: zhulihong@csust.edu.cn

Highlights

What are the main findings?

- A robust 2000–2025 impervious surface dataset was developed for Changsha County using consistent multi-sensor Landsat features and grouping strategies.
- Distinct three-phase expansion with edge-dominant growth and a northward hotspot shift was revealed, driven by a transition from natural constraints to socio-economic dominance.

What are the implications of the main findings?

- This study provides an empirical reference for understanding urbanization trajectories and driving-force transitions in similar rapidly developing counties.

Abstract

Long-term monitoring of impervious surface dynamics is essential for understanding urbanization processes and supporting sustainable land-use planning. However, existing studies often lack comprehensive analyses that integrate both spatial patterns and underlying driving mechanisms. In this study, we first generate a consistent long-term impervious surface dataset for Changsha County from 2000 to 2025 using Landsat time-series imagery, incorporating feature selection and temporal grouping to ensure reliability. Leveraging the generated long-term impervious surface dataset, we perform a detailed and multi-dimensional analysis of urban expansion, systematically quantifying changes in area, expansion intensity, and growth rate, while simultaneously examining spatial dynamics through centroid shifts and kernel density estimation, and uncovering underlying driving factors through rigorous modelling. The results indicate that impervious surface area increased continuously over the study period, with a clear phased pattern characterized by rapid growth (2000–2010), decelerated expansion (2010–2020), and further slowdown (2020–2025). Spatially, edge expansion dominates the overall growth (approximately 80%), while infilling gradually increases, indicating a transition from outward sprawl to more compact development. Moreover, expansion hotspots shift from the urban core to peripheral and rural areas, accompanied by a northward migration of the center of gravity. Driving factor analysis further indicates that topographic constraints weakened progressively over the study period, road proximity retained a stable spatial association with

Check for updates

Academic Editor: Victor Mesev

Received: 14 April 2026
Revised: 31 May 2026
Accepted: 14 June 2026
Published: 3 August 2026

Copyright: © 2026 by the authors. Licensee MDPI, Basel, Switzerland. This article is an open access article distributed under the terms and conditions of the Creative Commons Attribution (CC BY) license.

new impervious expansion as an accessibility-related proxy, and policy-related influences gained increasing importance in later stages. These findings provide new insights into the spatiotemporal evolution and driving mechanisms of county-level urbanization in central China, and offer a reliable methodological framework and scientific basis for long-term land-use monitoring and sustainable urban planning.

Keywords: county-level urbanization; impervious surface; land use planning; Landsat; spatiotemporal analysis; urban expansion

1. Introduction

With the rapid advancement of urbanization, urban expansion has become a major driver of contemporary global land-use change [1]. As the most direct and stable physical proxy for urbanization, impervious surfaces are critical for studies on land resource allocation, ecological security, hydrological modeling, and the urban heat island effect [2–5]. Therefore, long-term, systematic monitoring and analysis of impervious surfaces offer vital insights for spatial governance and coordinated urban-rural development [6–8].

Research on impervious surfaces has evolved from single-period area quantification to multi-temporal pattern analysis [9,10]. Remote sensing imagery has been widely used to analyze urban expansion patterns and spatial configurations [11,12], with a focus on balancing impervious surface growth with landscape connectivity for sustainable urbanization. Liu et al. employed morphological spatial pattern analysis and landscape connectivity methods to address the issue of balancing impervious surface expansion with landscape connectivity in county-level cities [13]. With the continuous development of research on Landscape Expansion Index (LEI), LEI and Expansion Intensity Index (EII) are now commonly employed to characterize the spatiotemporal dynamics of impervious surfaces and to decipher urban growth patterns [8,13,14]. Building on the LEI framework, researchers have developed derivative indices for more granular analysis. Zhang et al. [15] proposed a Landscape Evolution Characteristic Index, while He et al. [16] introduced a multidimensional LEI to quantify the compactness of impervious surface patches. In addition, analyses have been conducted using indicators such as the spatial distribution of land-use types, area growth rates, expansion intensity, hotspot analysis, and the identification of driving mechanisms [4,17]. As an important parameter characterizing the urbanization process, impervious surfaces are receiving increasing attention; however, most studies have focused on spatial resolution requirements [18], and systematic elucidation of long-term temporal evolution patterns remains insufficient.

The essence of urban expansion lies in a dynamic process characterized by phased development and path dependence [19]. To elucidate this transformation, research requires observing trajectory changes over extended time series, rather than relying solely on static comparisons between two points in time. Large-scale, long-term impervious surface strategies can mitigate accuracy issues associated with single- or multi-temporal imagery that are constrained by spatial resolution or intra-class spectral variability, and enable more reliable mapping of impervious surface coverage and changes at a large scale [6,20]. Several studies have adopted this long-term perspective. For instance, Kong et al. [7] examined spatiotemporal evolution patterns, Wang et al. [4] focused on area growth rates and expansion intensity, and Yin [6] mined long-term change information. However, most studies still rely primarily on single-dimensional analyses, such as urban LEI and impervious surface area change rates, resulting in a relatively narrow perspective on urbanization development within the study area.

Therefore, a multi-dimensional, integrated analytical framework is required to fully unravel the complex mechanisms of urban expansion. Spatiotemporal landscape indicators can reflect the morphology and trajectories of urban expansion [21], helping to identify expansion hotspots and cold spots. Centroid shift analysis in the study area can track the evolution and direction of urban form [22], enabling a macro-level understanding of the patterns of urban center migration. Meanwhile, kernel density estimation plays a crucial role in identifying the spatial clustering structure of development hotspots and their temporal changes. Classifying expansion rates into tiers can further characterize the growth gradients and spatial differentiation features of different regions. These indicators complement one another, collectively constructing a systematic analytical framework for urban expansion research across multiple dimensions, including quantity, direction, intensity and structure.

Based on a 25-year impervious surface time series (2000–2025) for Changsha County, this study conducts a comprehensive analysis of urban expansion, incorporating metrics such as area change, Expansion Intensity Index (EII), expansion rate, centroid shift, kernel density estimation, and driving factors. Emphasis is placed on the phased evolution of expansion mechanisms and spatial structures to reveal the dynamic processes underlying urban growth. By adopting a multidimensional analytical framework, this study aims to systematically characterize the spatiotemporal dynamics and stage-wise transformations of urban expansion in Changsha County, thereby providing deeper insights into the urbanization pathways of county-level cities in central China.

2. Materials and Methods

2.1. Study Area

Changsha County, administratively part of Changsha City, is located on the eastern bank of the lower Xiang River in eastern Hunan Province. It lies within the core area of the Changsha–Zhuzhou–Xiangtan (CZT) urban agglomeration. The county spans geographical coordinates from 112°56′E to 113°36′E and 27°55′N to 28°41′N. It covers a total area of approximately 1756 km^2 and comprises 5 subdistricts and 13 towns (Figure 1). It is one of the most representative regions for county-level economic development in central China. Since 2000, Changsha County has experienced rapid urbanization, characterized by industrial agglomeration and population inflows. This growth has made it a hotspot for construction land expansion and a consequent increase in impervious surface area [23]. However, systematic research on the long-term spatiotemporal evolution of impervious surfaces and their driving mechanisms in county-level regions remains limited [24], constraining a deeper understanding of the urbanization process and the formulation of spatially informed planning policies. Changsha County ranks among the top 100 counties nationally and leads the central and western regions in comprehensive development [13]. Despite its rapid urbanization, the county exhibits a relatively low degree of rural hollowing compared to other areas within the Changsha–Zhuzhou–Xiangtan (CZT) region [25]. In addition, the county encompasses a wide range of urbanization stages. Its built-up areas range from highly saturated central urban districts to rapidly transforming suburban fringe zones, and to remote rural areas where new development has only recently begun. This diversity of urbanization stages within a single county provides a valuable opportunity to study how urban expansion processes vary across different spatial contexts. Accordingly, investigating the spatial patterns of expansion, stage-specific expansion modes, and the temporal evolution of driving factors is important for understanding urban expansion and land resource utilization in county-level areas of central China. Given its developmental trajectory and these characteristics, Changsha County serves as an illustrative case for analyzing county-level urbanization in central China.

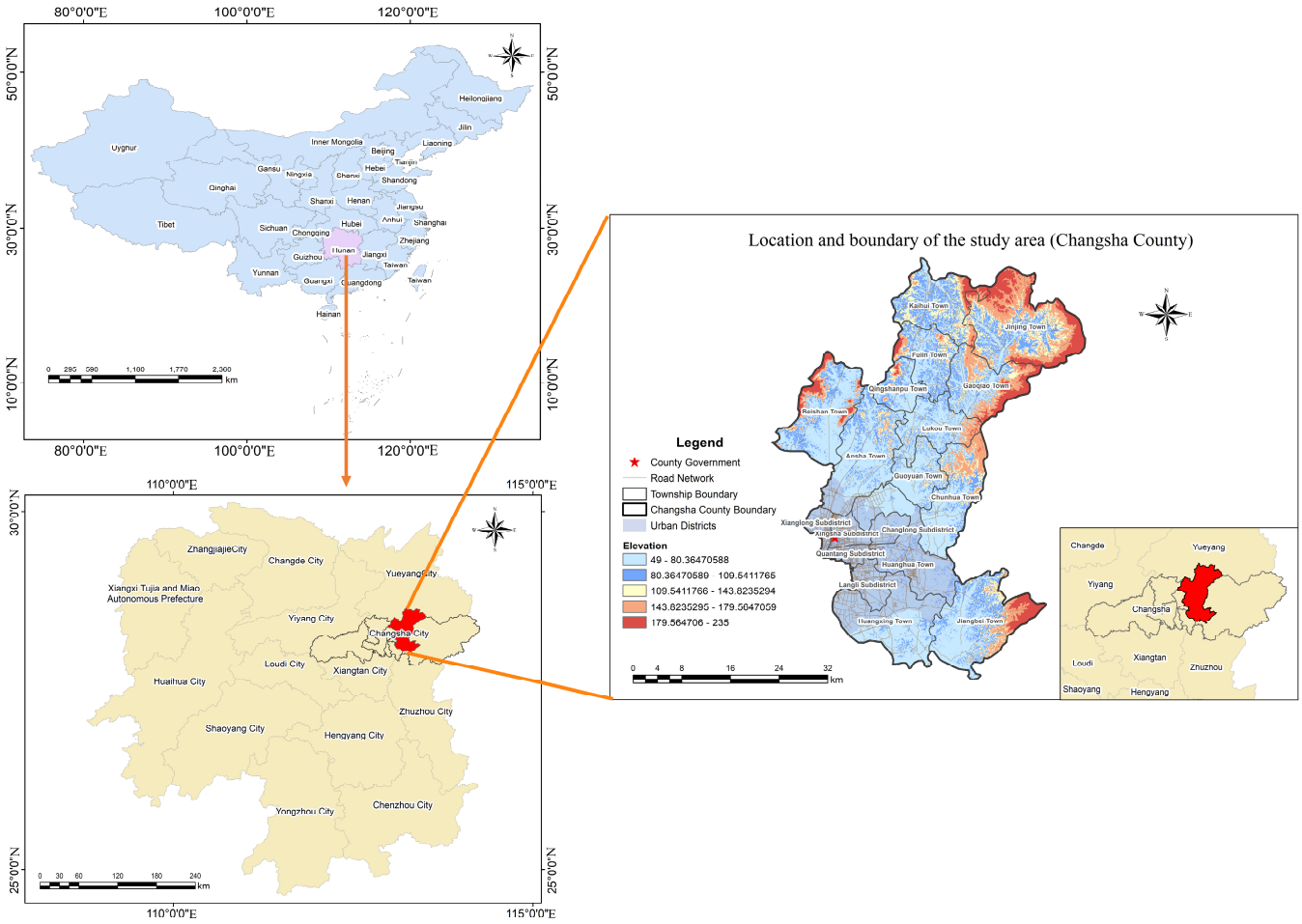


Figure 1. Location and elevation of the study area (Changsha County, Hunan Province, China). The main figure shows the administrative boundaries, township divisions, road network, and elevation distribution of Changsha County. The two insets illustrate the location of Hunan Province within China (**top left**) and the location of Changsha County within Hunan Province (**bottom left**). Elevation is shown with a blue–yellow–red ramp; the legend lists discrete hypsometric intervals.

2.2. Technology Roadmap

The overall workflow comprises data pre-processing and feature extraction, impermeable surface classification and long-term time-series analysis (Figure 2). To mitigate interannual fluctuations caused by atmospheric conditions and sensor variations [26,27], the study period was divided into three main intervals: 2000–2010, 2010–2020 and 2020–2025, with the final interval spanning five years to align with the conclusion of the time series. All core analyses were conducted for these three main periods to provide a consistent temporal framework for long-term comparison and to reduce the influence of annual image-quality fluctuations. In addition, Annual, four-year, and five-year analyses were retained as supplementary fine-scale analyses to reveal spatial heterogeneity and transitional details within and across the main stages. These finer-scale results were not used as a substitute for the primary-period trends. Periods affected by Landsat 7 data-quality issues were interpreted cautiously and further evaluated through uncertainty propagation and gap-filled versus observed-pixel comparison. Finally, sensitivity analyses were conducted to assess whether the observed directional patterns were merely short-term artifacts of the 2020–2025 period.

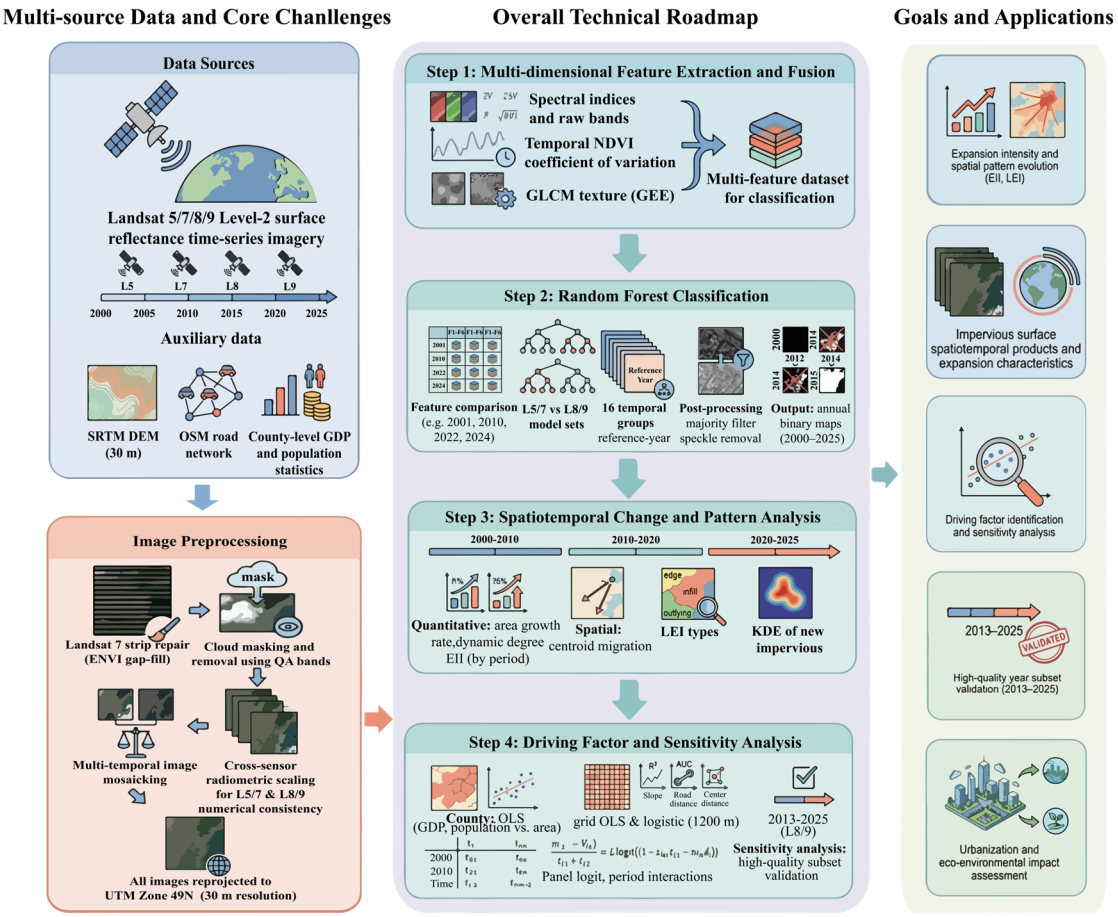


Figure 2. Full Methodological Framework: Multi-Source Data Processing, Challenge Mitigation, and Technical Workflow for 2000–2025 Impervious Surface Classification, Spatiotemporal Analysis, and Driving Factor Assessment.

2.3. Data and Preprocessing

Landsat 5/8/9 Level-2 surface reflectance imagery from the Google Earth Engine (GEE) platform served as the primary data source. Landsat 7 imagery was downloaded directly from the USGS, gap-filled using ENVI 5.6 software, and then imported into GEE for unified processing with the other datasets. The imagery covers the period from 2000 to 2025, comprising 24 scenes. Data for 2012 and 2014 are unavailable due to the operational transition between Landsat 5 and Landsat 8, which left no scenes meeting the quality standards required for this study. Because the default administrative boundaries in GEE show positional inaccuracies at the county scale, boundary data for Changsha County was obtained from DataV.GeoAtlas to define a consistent spatial extent for all subsequent image cropping, grid generation and spatial analyses. Socioeconomic data (Gross Domestic Product, GDP; registered population) for subsequent driving factor analysis were sourced from the Changsha County Statistical Bulletin and Statistical Yearbook. Digital Elevation Model (DEM) data were obtained from the 30-m resolution ASTER GDEM V3 product via the Geospatial Data Cloud. Road network data were sourced from the Hunan Province road network vector data in OpenStreetMap (OSM). Because consistent annual historical road-network data were not available, the road network was treated as a static accessibility layer to represent proximity to major transport corridors, rather than as a year-specific record of road construction.

All imagery was preprocessed prior to use. For available imagery from July to September of each year, an adaptive compositing strategy was employed on the GEE platform:

for years with minimal cloud cover, annual composite data was generated primarily from high-quality imagery. For cloudy years, all valid images from this period were utilized for compositing to maximize spatial coverage. Following striping correction and cropping of Landsat 7 imagery, the subsequent mosaicking and export procedures were consistent with those applied to the Landsat 5/8/9 imagery. To promote radiometric consistency across sensors [28], all data were exported using identical thresholds for clipping maximum reflectance values. The impervious surface classification outputs and all auxiliary datasets were reprojected to the UTM Zone 49N coordinate system at a uniform 30 m spatial resolution, thereby minimizing spatial distortion and supporting subsequent spatial analyses.

2.4. Feature Construction and Selection

Impervious surfaces were extracted from Landsat surface reflectance imagery by constructing a suite of spectral, textural, and raw band features [29]. To improve separability between impervious surfaces and other land covers (e.g., vegetation, water, bare soil), a set of spectral indices was computed. These included the Normalized Difference Vegetation Index (NDVI), the Normalized Difference Built-up Index (NDBI), the Normalized Difference Moisture Index (NDMI), the Modified Normalized Difference Water Index (MNDWI), the Soil-Adjusted Vegetation Index (SAVI), and the Bare Soil Index (BSI). Texture features (energy, contrast, homogeneity, entropy, and dissimilarity) were calculated based on the Gray-Level Co-occurrence Matrix (GLCM). The GLCM was applied to the near-infrared (B4/B5) and short-wave infrared (B6/B7) bands using a 7×7 pixel moving window to quantify the local spatial heterogeneity associated with impervious surfaces. The surface reflectance values of the core optical bands were retained as direct spectral inputs, following the band specifications of each sensor series (B1–B5, B7 for Landsat 5/7; B2–B7 for Landsat 8/9).

To assess the robustness and temporal stability of the feature set across the Landsat sensor series, a representative year with high-quality imagery was chosen for each sensor platform: 2001 (Landsat 5), 2010 (Landsat 7), 2022 (Landsat 8), and 2024 (Landsat 9). Based on these representative years, six distinct feature sets were designed and compared to identify an optimal configuration for long-term classification: F1 included Spectral indices only, F2 included Spectral indices + raw bands, F3 included Spectral indices + texture features, F4 included All features (spectral + texture + raw bands), F5 was the optimal subset selected from F4 via Recursive Feature Elimination with Cross-Validation (RFECV, 5-fold), F6 was Top 10 features ranked by importance (derived from F4).

Considering the differences in bandpass characteristics between the Landsat 5/7 and Landsat 8/9 sensors, two sensor-specific fixed feature sets were established. Each set comprised the top 10 features (ranked by importance) derived from the representative year of the corresponding sensor series: 2010 (Landsat 7, representing Landsat 5/7) and 2022 (Landsat 8, representing Landsat 8/9). This approach aimed to promote consistency within each sensor family and to mitigate the effects of inter-annual spectral variation and cross-sensor domain shift.

2.5. Classification and Accuracy Assessment

In this study, a binary classification system was adopted. The impervious surface class includes human-made materials that prevent water infiltration, such as asphalt and concrete roads, building rooftops, parking lots, and other anthropogenic structures. The pervious surface class includes vegetation, water bodies, and bare soil (including agricultural land, sandy areas, and exposed soil). Sample points were annotated through visual interpretation of the imagery and distributed uniformly across the study area. The

total number of samples for each benchmark year ranged from approximately 686 to 1000, depending on image quality. The samples were then randomly split into a training set (70%) and an independent validation set (30%). To ensure balanced class distributions and reproducible train/validation splits across years, we developed a custom Python 3.10 script with an adaptive tolerance threshold (5%, Supplementary Table S1) to maintain an approximate 7:3 train/validation ratio and a 1:1 impervious/pervious balance within each split.

The Random Forest (RF) algorithm was employed for model training and classification [4], due to its robustness to high-dimensional data and its ability to estimate feature importance [29]. Feature importance was quantified using the mean decrease in Gini impurity (Gini importance). Two distinct Random Forest configurations were used for different purposes. For feature evaluation and selection, we used 300 decision trees (n_estimators = 300) with a limited maximum depth (max_depth = 10) to stabilize the estimates of feature importance and RFECV results. For the final time-series classification, we used 100 trees (n_estimators = 100) with no depth constraint to balance classification accuracy and computational efficiency [30]. Overall Accuracy (OA), the Kappa coefficient, and five-fold stratified cross-validation were used to evaluate the six feature combinations on representative years to determine the optimal and most consistent feature combination. For the complete time series (2000–2025), two sensor-specific sets of the top 10 features were used to divide the study period into 16 groups, with a reference year designated for each group (Supplementary Table S2). For non-representative years, samples were preferentially migrated from the nearest high-quality reference year within the same sensor group and manually verified and corrected by the same interpreter using the corresponding-year Landsat imagery and high-resolution imagery. A model trained on each group's reference-year samples was then applied to classify all years within that group. For each benchmark (reference) year, model performance on the independent validation set was assessed using OA, the Kappa coefficient, and F1-score. Confusion matrices and per-year sample numbers and class composition are provided in Supplementary Figure S1.

To evaluate the effect of gap-filling on classification reliability, two representative Landsat 7 years (2007 and 2015) were selected. Based on per-pixel data availability in pre-fusion single-scene imagery, pixels in the final maps were divided into gap-filled regions (no valid observation before gap-filling) and originally observed regions (valid observation before gap-filling). Impervious-surface pixel proportions and sample-based accuracy metrics (OA, Kappa coefficient, and F1-score) were calculated separately for the two subsets. Because validation samples in gap-filled regions were limited (N = 12 in 2015), this comparison was treated as supporting diagnostic evidence rather than as an independent estimate of overall accuracy in gap-filled areas.

2.6. Spatiotemporal Analysis

2.6.1. Analysis of Spatiotemporal Patterns and Dynamic Indices

Changes in impervious surface area (km^2) and its proportion were analyzed based on statistics of valid pixels from the annual impervious surface grids. To maintain consistency between area and proportion measures, the annual impervious area time series was used to calculate the area growth rate (G) and the annual dynamic degree (K) for both consecutive years and multi-year periods. The total impervious area for a given year was calculated as:

$$U = N \times r^2 \quad (1)$$

where U is the total impervious area (km^2), N is the count of impervious pixels, and r is the pixel side length (km). The area growth rate (G, in %) and the dynamic degree (K, in %) are defined as:

$$G = \frac{U_b - U_a}{U_a} \times 100\% \quad (2)$$

$$K = \left[\frac{U_b - U_a}{U_a}\right] \times \left(\frac{1}{T}\right) \times 100\% \quad (3)$$

where U_a and U_b are the impervious areas at the start and end of a period, respectively, and T is the length of the period in years. The dynamic degree K represents the mean annual relative change rate, enabling comparison across periods of varying lengths. Supplementary annual and five-year analyses followed the temporal framework in Section 2.2. To assess the reliability of net area changes between periods, an uncertainty propagation analysis was applied to the mapped areas derived from Equations (1)–(3). Single-year area uncertainties were estimated from classification accuracy using two alternative metrics, (1 − OA) and (1 − F1-score; Supplementary Table S3). Propagated uncertainty for each period was calculated as:

$$\sigma_{\text{prop}} = \sqrt{\sigma_{\text{start}}^2 + \sigma_{\text{end}}^2} \quad (4)$$

where σ_{start} and σ_{end} are the single-year area uncertainty estimates for the start and end years, respectively. Periods with absolute net changes smaller than σ_{prop} were interpreted as having signals that fall within the classification uncertainty range, and their directional interpretations were treated with caution.

2.6.2. Assessment of Expansion Intensity and Spatial Heterogeneity

The expansion intensity within the study area was assessed. This was done by normalizing the change in impervious area relative to the total area of the study region and the length of the time period, which facilitates comparisons across different time periods and geographical areas. The resulting Expansion Intensity Index (EII) values were classified into five levels: Slow (0–0.28), Low (0.28–0.59), Medium (0.59–1.05), Fast (1.05–1.92), and High (>1.92). In addition to the three primary periods, the EII was also computed for five-year and annual intervals. The EII for a given spatial unit was calculated as:

$$EII = \frac{U_b - U_a}{A} \times \frac{1}{T} \times 100\% \quad (5)$$

where U_a and U_b are the impervious surface areas at the beginning and end of the period (km^2), A is the total area of the spatial unit (km^2), and T is the length of the period in years.

In parallel, spatial analysis of expansion rates was performed using calculations for each grid cell at the grid scale, followed by classification and mapping to reveal the spatial heterogeneity of expansion intensity and the distribution of hotspots across different time periods. The expansion rate (v_i, in km^2 yr^{-1}) for grid cell i is defined as:

$$v_i = \frac{\Delta U_i}{T} = \frac{U_{b,i} - U_{a,i}}{T} \quad (6)$$

where $U_{a,i}$ and $U_{b,i}$ are the impervious surface areas within grid cell i at the start and end of the period (km^2), and T is the period length in years.

2.6.3. Classification of New Impervious Areas Using the Landscape Expansion Index (LEI)

The LEI was employed to classify the spatial growth pattern of newly added impervious pixels. A pixel-level overlay was performed on impervious surface grids from consecutive periods. Each pixel was assigned to one of four categories: stable non-impervious, newly impervious, water-impervious conversion, and stable impervious. Newly impervi-

ous pixels were aggregated into connected patches for LEI analysis. Following the original definition of the LEI [31], a buffer around each patch was generated by morphological dilation with a 3 × 3 pixel structuring element (i.e., a one-pixel buffer, corresponding to 30 m, the spatial resolution of the Landsat data) [32]. The same buffer configuration was applied consistently to all periods. For each patch, let R denote the ratio of buffer pixels overlapping pre-existing impervious surface to the total number of buffer pixels:

$$R = \frac{L_o}{L_{total}} \tag{7}$$

where L_o is the area of intersection between the buffer zone and the pre-existing impervious surface, and L_{total} represents the total area of the buffer zone. Patches were classified as Infilling ($R > 0.5$), Edge expansion ($0 < R \leq 0.5$) or Outlying ($R = 0$), and the area and number of patches were then summarized for each growth type. In addition to the primary three-period analysis, a more detailed analysis was conducted by year and by sub-area.

2.6.4. Centroid Shift Trajectory and Kernel Density Estimation (KDE)

A centroid shift analysis was conducted for the study area. The centroid coordinates (X_c, Y_c) of impervious surfaces for each year were calculated as the arithmetic mean of the coordinates of all impervious pixels (UTM Zone 49N projection):

$$X_c = \frac{\sum x_i}{N}, Y_c = \frac{\sum y_i}{N} \tag{8}$$

where x_i and y_i are the coordinates of the i-th impervious pixel, and N is the total number of impervious pixels. The centroid displacement distance (D, in m) and azimuth (A, in degrees) between consecutive or key years were calculated from the coordinate differences. The trajectory of centroid movement was subsequently visualized.

The kernel density estimation (KDE) was performed using the newly added impervious pixels identified from the difference between the start- and end-year grids, thereby generating density surfaces to visualize the spatial intensity of expansion for each time period.

2.7. Multi-Scale Modeling of Driving Factors

Regression analysis was conducted to examine the relationship between impervious surfaces and GDP and registered population at the county level. A multiple linear regression model was constructed with total impervious area as the dependent variable and GDP and registered population as independent variables. To assess potential collinearity between GDP and population, univariate regression diagnostics were performed separately, and a model was fitted using the natural logarithms of the variables to mitigate heteroscedasticity.

To balance statistical power with spatial granularity, a grid scale of 1200 m was selected as the analysis unit based on multi-scale sensitivity tests. Using the number of newly added pixels and binary variables within the grid as dependent variables, and slope, distance to the nearest road, and distance to the county town center (using the location of Changsha County People's Government as the reference, 113.081097°E, 28.246918°N) as independent variables, linear regression (assessed by R^2) and logistic regression (assessed by the Area Under the Curve, AUC) models were constructed respectively.

The study area was divided into three time periods for comparison, and grid data from each period were merged to construct a panel dataset. Time-period dummy variables (with 2000–2010 as the baseline) and their interaction terms with geographical drivers were introduced to a panel logistic regression model, which was then specified to test for

temporal differences in the effects of geographical drivers across different time periods. The form of the panel logistic regression model is:

$$\begin{aligned}\log\left(\frac{p}{1-p}\right) = \beta_0 &+ \beta_1 \cdot slope + \beta_2 \cdot road + \beta_3 \cdot center + \gamma_2 \cdot D_{2010-2020} \\ &+ \gamma_3 \cdot D_{2020-2025} + \delta_{12} \cdot (slope \times D_{2010-2020}) + \delta_{13} \\ &\cdot (slope \times D_{2020-2025}) + \delta_{22} \cdot (road \times D_{2010-2020}) + \delta_{23} \\ &\cdot (road \times D_{2020-2025}) + \delta_{32} \cdot (center \times D_{2010-2020}) + \delta_{33} \\ &\cdot (center \times D_{2020-2025}) + \varepsilon\end{aligned} \quad (9)$$

where $D_{2010-2020}$ and $D_{2020-2025}$ are time-period dummy variables, and the interaction coefficients δ_{jk} represent the change in the effect of the corresponding variable relative to the reference time period. The statistical significance of an interaction term is tested to assess whether the influence of the corresponding geographical driver differed significantly between that period and the baseline period.

2.8. Sensitivity Analysis

Sensitivity analyses were conducted to examine the influence of grid scale selection and analysis-period length on the primary conclusions of the driving-factor analysis.

Grid-scale sensitivity analysis was conducted using the 2020–2025 period as an example, because recent impervious-surface expansion was more spatially dispersed and therefore more sensitive to the choice of aggregation unit. Linear and logistic regression models were fitted at six candidate grid sizes (200, 500, 800, 1000, 1200, and 2000 m). The comparison considered the number of grid cells, the proportion of expansion cells, linear R^2, logistic AUC, and the coefficient directions of slope, distance to roads, and distance to the county center. The objective was not to maximize a single metric, but to identify an analytical scale that balanced sample size, model performance, coefficient stability, and spatial granularity.

To assess whether the directional patterns identified for 2020–2025 reflected a short analysis window rather than a robust later-stage signal, the driving-factor models were re-estimated for the extended period 2013–2025 and compared with those for 2020–2025. Because 2013–2025 spans a longer recent interval that still includes the final primary period, consistency between the two model sets provides a check on short-window sensitivity rather than a test of image-quality differences alone. Consistency in coefficient signs and similarity in AUC values between the two periods were used to evaluate whether the 2020–2025 results were attributable solely to the five-year window.

2.9. Key Methodological Features

The workflow above includes several design choices that support the consistency and reliability of the long-term impervious-surface time series. Rather than re-selecting features annually, we fixed the top-10 feature set for each sensor family (Landsat 5/7 and Landsat 8/9) using representative years, prioritizing temporal comparability over year-specific accuracy (Section 2.4). For non-reference years, samples were migrated from the nearest reference year within the same sensor group and manually verified using corresponding-year Landsat imagery and high-resolution imagery (Section 2.5). Classification accuracy metrics (OA and F1-score) were further propagated to bound area-change uncertainty and distinguish robust primary-period trends from shorter intervals more sensitive to mapping error (Section 2.6.1). Analyses were organized around three primary periods (2000–2010, 2010–2020, and 2020–2025), with annual and four-year results retained for supplementary spatial detail (Section 2.2), and sensitivity tests applied to grid scale and analysis-period length (Section 2.8).

These choices are not presented as methodological innovations, but as pragmatic adaptations to the challenges of multi-sensor, long-term impervious-surface mapping.

3. Results

3.1. Feature Importance and Classification Performance

The performance of the six feature sets (F1–F6) was evaluated on the representative years using sensor-specific top-10 feature sets. Spectral indices and raw bands were the dominant contributors. The top-ranking features in each representative year were primarily from these categories (B3 in 2001, B7 in 2010, and B2 and B4 in 2022 and 2024), with NDVI consistently ranking among the top performers (Figure 3). However, the F1 sets using only these two feature categories showed the lowest temporal stability. F2 improved accuracy but lacked spatial structural information (Figure 4). Although it was able to identify high-density built-up areas relatively well in urban regions, the boundaries of built-up areas in peri-urban and rural regions were fragmented (Figure 5). F3 yielded more continuous boundaries, but excessive smoothing reduced detail in urban, rural, and mountainous areas. The full feature set F4 achieved slightly higher accuracy and improved detection of rural buildings along roads, but feature redundancy raised overfitting concerns and increased computational cost. F6 retained the core structure of F4 while keeping overall accuracy within ±1.5% of F4; by reducing dimensionality from 35 to 10 features, it provided a practical balance between efficiency and stability and was therefore adopted for subsequent long-term classification.

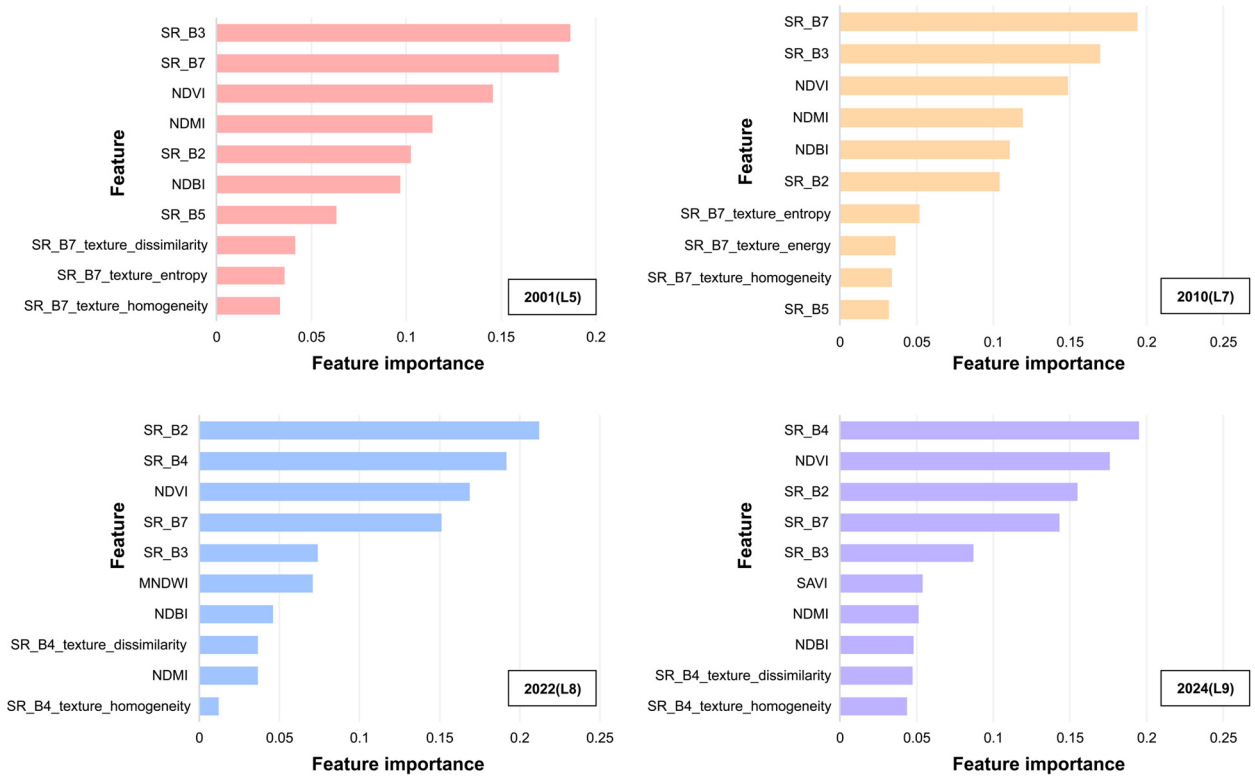


Figure 3. Feature importance of the top 10 variables for impervious surface classification across four representative years with corresponding Landsat sensors.

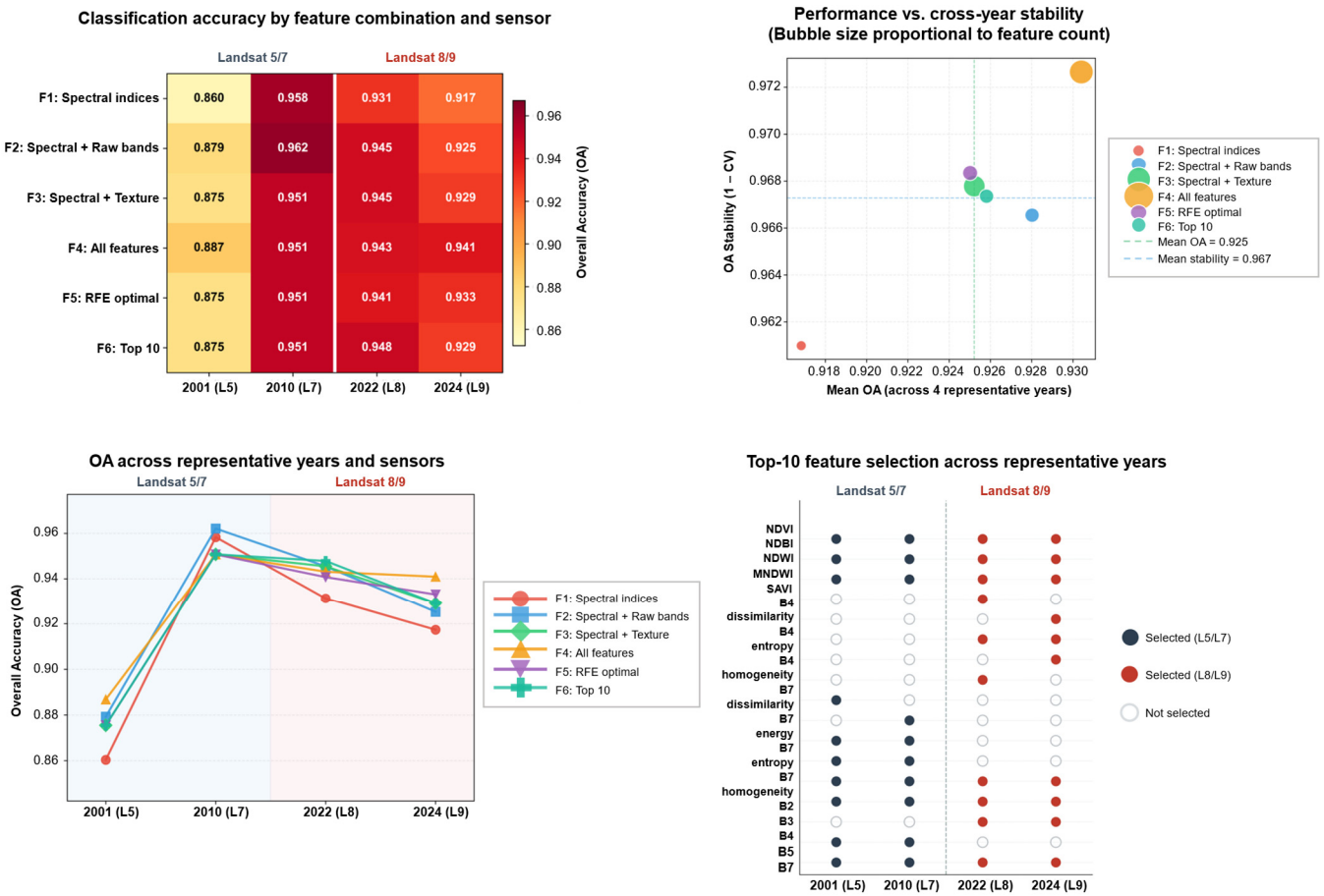


Figure 4. Robustness assessment of six feature combinations (F1–F6): classification accuracy and temporal stability for long-term impervious surface mapping using multi-sensor Landsat data.

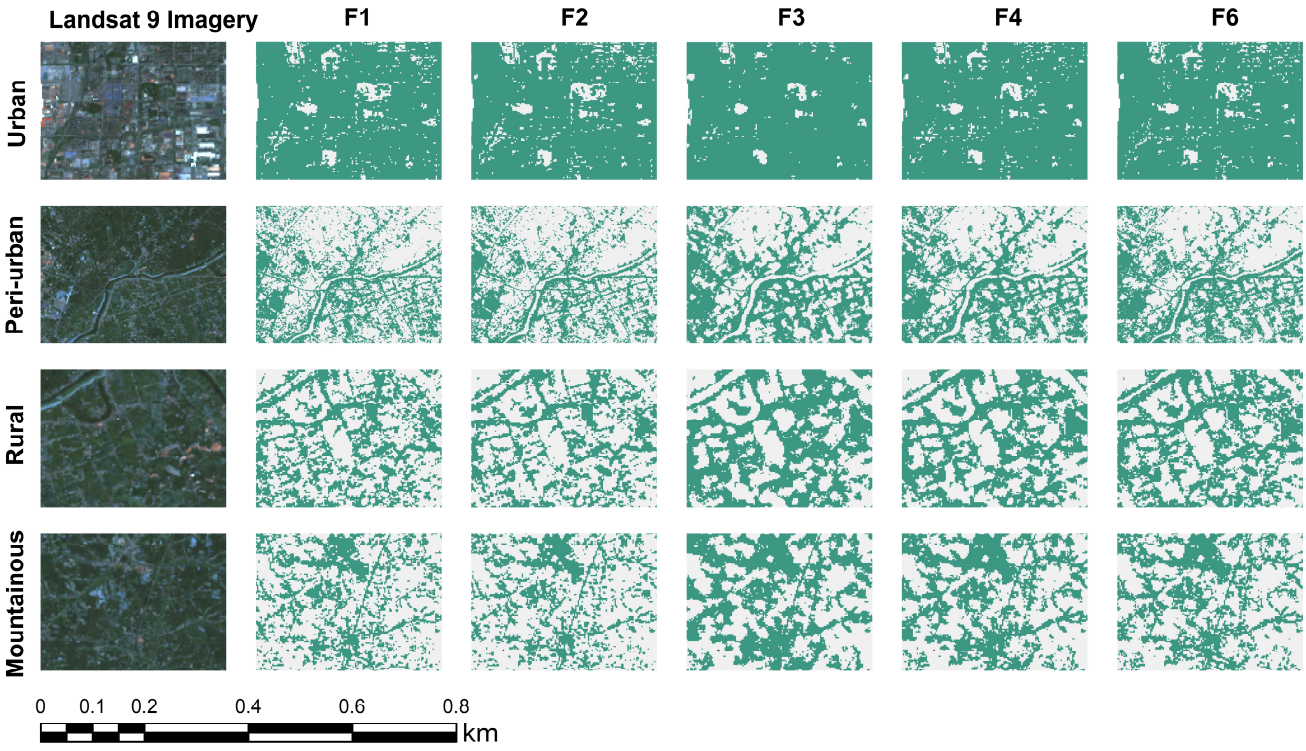


Figure 5. Visual comparison of impervious surface classification results from selected feature combinations across four typical landscape types using Landsat 9 imagery.

After F6 and the sensor-specific Top-10 feature sets were fixed, annual impervious-surface maps for 2000–2025 were produced using the grouped long-term classification workflow (Section 2.4). Independent validation on the benchmark year of each group yielded a mean OA of 91.44%, mean Kappa of 0.8394, and mean F1-score of 0.9150 (Supplementary Table S1, Supplementary Figure S1). These aggregate metrics, however, do not indicate where classification errors occur.

Classification errors were spatially non-uniform and concentrated in two landscape settings (Figure 5): in the densely populated western areas, scattered non-impervious patches amidst buildings were frequently misclassified; in the northern mountainous areas, isolated buildings and small settlements located near roads were similarly affected. Furthermore, the suboptimal image quality of Landsat 5 and Landsat 7 (notably Landsat 7) exacerbated this issue, making it difficult to accurately deploy sample points in the aforementioned areas through visual interpretation. To address this, the dominant years for Landsat 5 and Landsat 7 were further subdivided during grouping (Table S1), which effectively mitigated the overestimation of impervious surface cover values (reducing them from 42–50% to approximately 20%), although some residual variability remained.

For two representative Landsat 7 years (2007 and 2015), gap-filled and originally observed regions were compared (Supplementary Table S4). At the pixel level, impervious proportions were consistently higher in gap-filled than in originally observed regions, by 3.77 and 4.88 percentage points in 2007 and 2015, respectively. Sample-based validation for 2015 showed the same pattern, with lower OA and Kappa in gap-filled areas (0.8333 vs. 0.9565 and 0.6364 vs. 0.9130, respectively; N = 12). Because only a limited number of validation samples fell within gap-filled regions, these sample-level metrics were treated as diagnostic evidence. Taken together, both comparisons indicate higher impervious estimates and lower classification reliability in gap-filled regions.

3.2. Temporal Dynamics and Expansion Intensity of Impervious Surfaces

The impervious area in the study area increased from approximately 480 km^2 in 2000 to approximately 758 km^2 in 2025, representing a net increase of 278 km^2 and an average annual gain of about 11 km^2 (Figure 6, Supplementary Table S5). The overall trend was upward, but significant interannual fluctuations are evident in the time series (Figure 7), primarily attributable to variations in image quality and classification errors. The rate of impervious area expansion decelerated gradually across the three primary time periods (Supplementary Table S6). The period from 2000 to 2010 was characterized by rapid urbanization, with an area increase of approximately 178 km^2 and the dynamic degree (K) of 3.7%. From 2010 to 2020, the expansion slowed (approximately 78 km^2), with K falling to 1.2%, whilst from 2020 to 2025, the expansion moderated further (22 km^2). When analyzed in five-year intervals (Table 1), the increase in area decreased from 357 km^2 in 2000–2005 to 180 km^2 in 2020–2025, whilst the net increase narrowed from 239 km^2 to 22 km^2, consistent with the trend of declining growth rates.

To evaluate the reliability of the mapped area changes, uncertainty-propagation results are reported in Supplementary Table S3. For 2005–2010, the mapped net decrease (-61.4 km^2) represented 47–51% of the propagated uncertainty range (121–130 km^2); for 2015–2020, the mapped net decrease (-2.95 km^2) represented approximately 5% of the propagated uncertainty range (56–57 km^2). Neither semi-decadal apparent decrease exceeded the propagated classification-uncertainty bounds. By contrast, the net increases for the primary periods 2000–2010 (+177.9 km^2) and 2010–2020 (+78.0 km^2) were 2.29–2.52 and 1.81–1.87 times the propagated uncertainty range, respectively, whereas the 2020–2025 net increase (+21.6 km^2) was approximately 33% of the corresponding range.

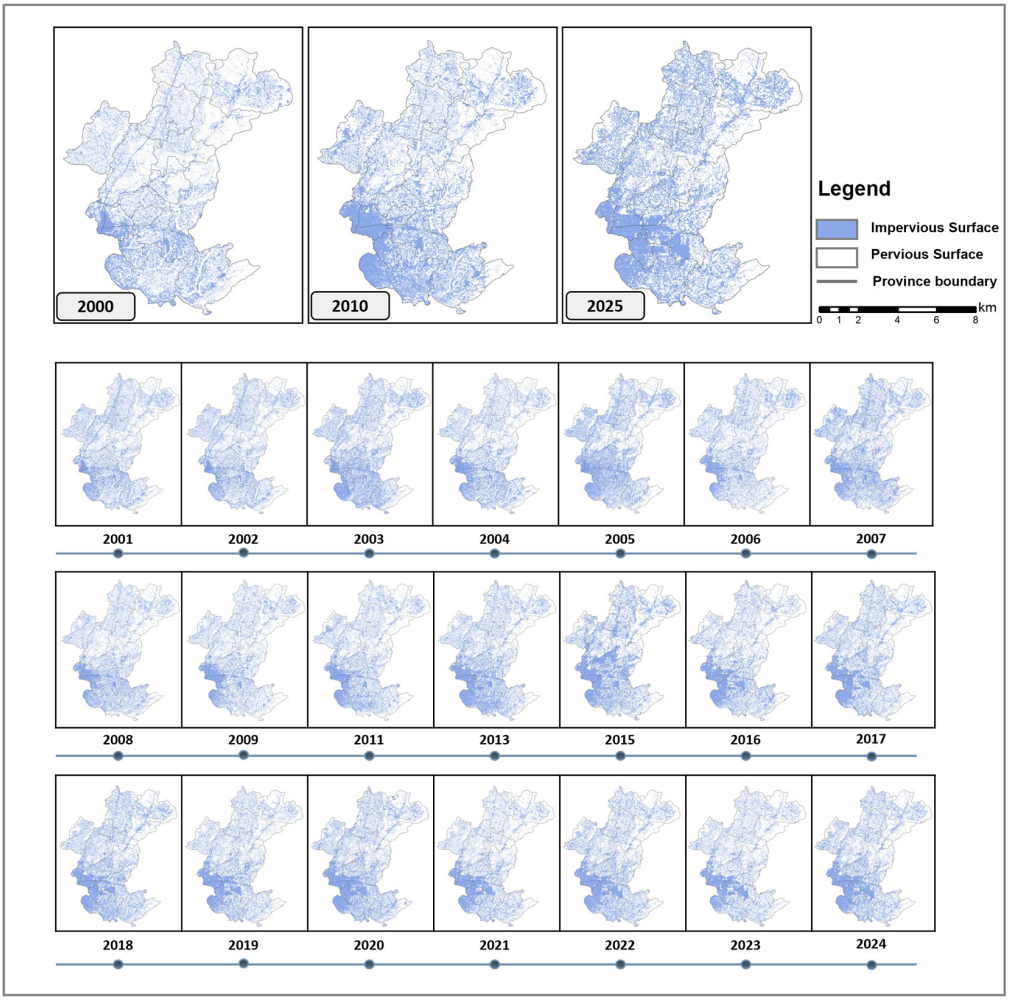


Figure 6. Spatiotemporal distribution and annual dynamics of impervious surfaces in the study area, 2000–2025.

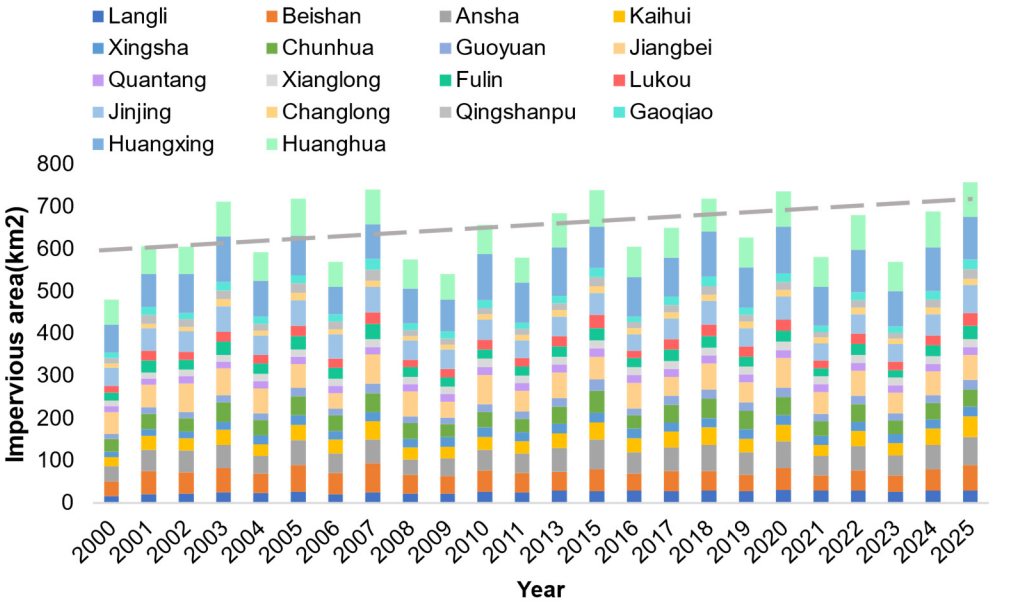


Figure 7. Inter-annual dynamics of impervious surface area and township-level composition in the study area, 2000–2025.

Table 1. Gains and losses of impervious surface area in Changsha County from 2000 to 2025 (km^2).

Period	New Impervious	Loss Impervious	Total
2000–2005	357.3	118.0	239.3
2005–2010	185.9	247.0	−61.1
2010–2015	263.1	182.3	80.8
2015–2020	198.5	201.3	−2.8
2020–2025	180.0	157.9	22.1

Changes in the Expansion Intensity Index (EII) further clearly illustrate the phased deceleration of urban expansion (Figure 8a). The EII values for the three periods were 1.01 (moderate), 0.44 (low) and 0.25 (slow). However, the annual EII fluctuated sharply, frequently alternating between positive and negative values (Figure 8b, Supplementary Table S7). In contrast, the 10-year-scale EII, by averaging over a longer period, effectively dampened these annual fluctuations and revealed a more stable declining trend.

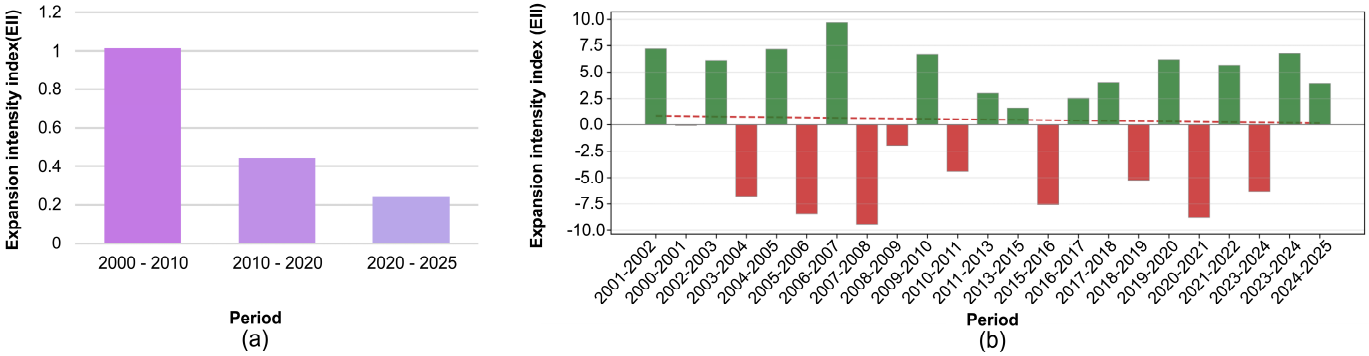


Figure 8. Temporal dynamics of impervious surface expansion intensity index (EII) in the study area, 2000–2025: (**a**) EII for three key study periods; (**b**) inter-annual EII variations, where green columns indicate positive growth, red columns indicate negative growth, and the red dashed line shows the overall trend.

Spatially, the expansion rates at the grid scale delineate the shifting trajectory of hotspots over time (Figure 9). From 2000 to 2010, a center-periphery pattern emerged, with the Xingsha–Huangxing–Langli line serving as the core, from which activity diminished outward. From 2010 to 2020, the hotspots shifted from the center towards the north and south; Huanghua Town (13.3 km^2) led in new growth, whilst Jinjing (7.0 km^2) and Kaihui (9.7 km^2) in the north began to emerge. From 2020 to 2025, the expansion hotspots shifted further outwards to the county's periphery. Jinjing (12.1 km^2) and Kaihui continued growing, becoming the largest areas of new expansion, whilst Beishan Town (8.2 km^2) and Fulin Town (5.7 km^2) also experienced growth. In contrast, there were no new growth areas in the central urban core or its immediate suburbs. This pattern highlights an ongoing shift of expansion hotspots from the urban core toward the distant rural periphery.

3.3. Spatial Expansion Patterns

The dominant expansion patterns across the county were analyzed using the annual distribution of Landscape Expansion Index (LEI) values (Figure 10a, Supplementary Table S8) and data aggregated over three primary time periods (Figure 10b). Both analyses indicated that edge expansion predominated in Changsha County, followed by infilling, whilst outlying areas accounted for a relatively small proportion. Between 2000 and 2010, edge expansion accounted for 89% of the total area of the three types, infilling for approximately 8%, and outlying for approximately 2%. During 2010–2020, edge expansion, infilling and outlying accounted for approximately 86%, 11% and 3% respectively. For

2020–2025, the corresponding proportions were 81%, 16% and 2%. The edge expansion accounted for more than 80% in all three periods, indicating that edge expansion was the dominant mode of urban expansion in Changsha County during the study period.

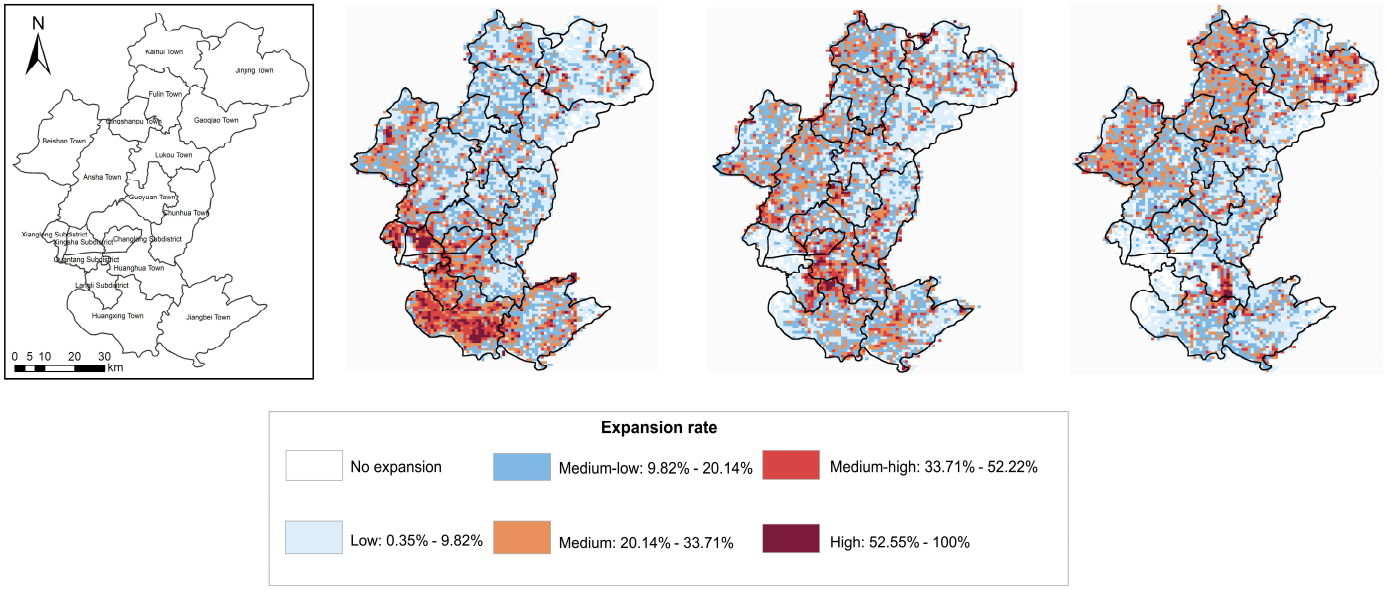


Figure 9. Spatial distribution of expansion speed grades at the grid scale for the three periods, arranged chronologically from (**left**) to (**right**) (2000–2010, 2010–2020, 2020–2025).

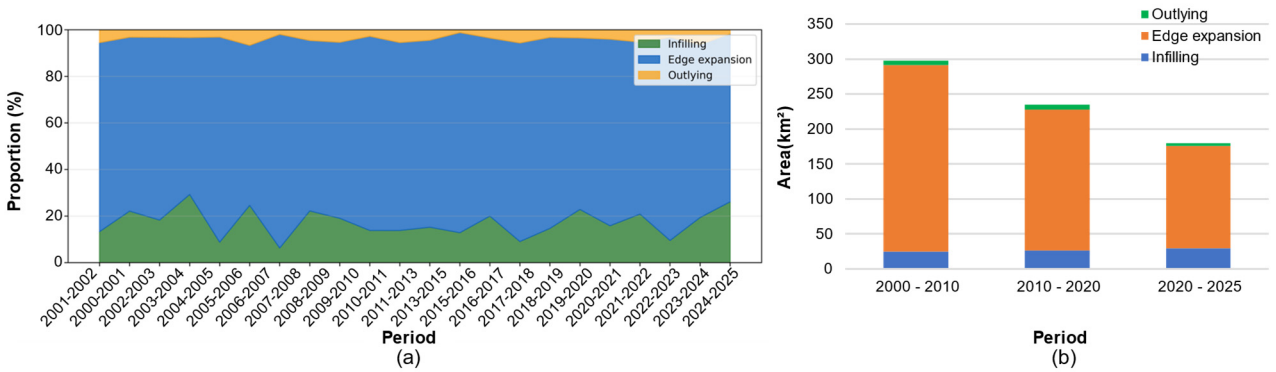


Figure 10. Impervious surface landscape expansion patterns in the study area, 2000–2025: (**a**) inter-annual distribution of expansion types (infilling, edge expansion, outlying); (**b**) area statistics of expansion patterns across three key study periods.

The four-year LEI maps (Figure 11) provide supplementary fine-scale detail on how infilling, edge, and outlying expansion evolved within each development stage, while the three primary periods remain the basis for the main quantitative trends (Section 2.2). The case-study insets illustrate these shifts at the local scale. In the central area near the county government (inset a), scattered infilling patches in later years are embedded within the existing built-up fabric, surrounded by earlier edge-expansion areas and less extensive later-stage edge growth. This pattern suggests internal land-use intensification after decades of outward expansion and appears consistent with recent regional emphasis on more compact urban development. By contrast, the Guoyuan–Ansha interface in the mid-county peri-urban zone (inset b) showed more continuous edge expansion and scattered outlying patches in the middle and late periods, reflecting active peripheral growth within Changsha County under the county's multi-node spatial development layout. In the northernmost window of Jinjing Town (inset c), larger and more isolated outlying patches emerged during

2013–2021, highlighting scattered expansion in the distant periphery in townships where rural revitalization and eco-tourism development have been promoted in recent years.

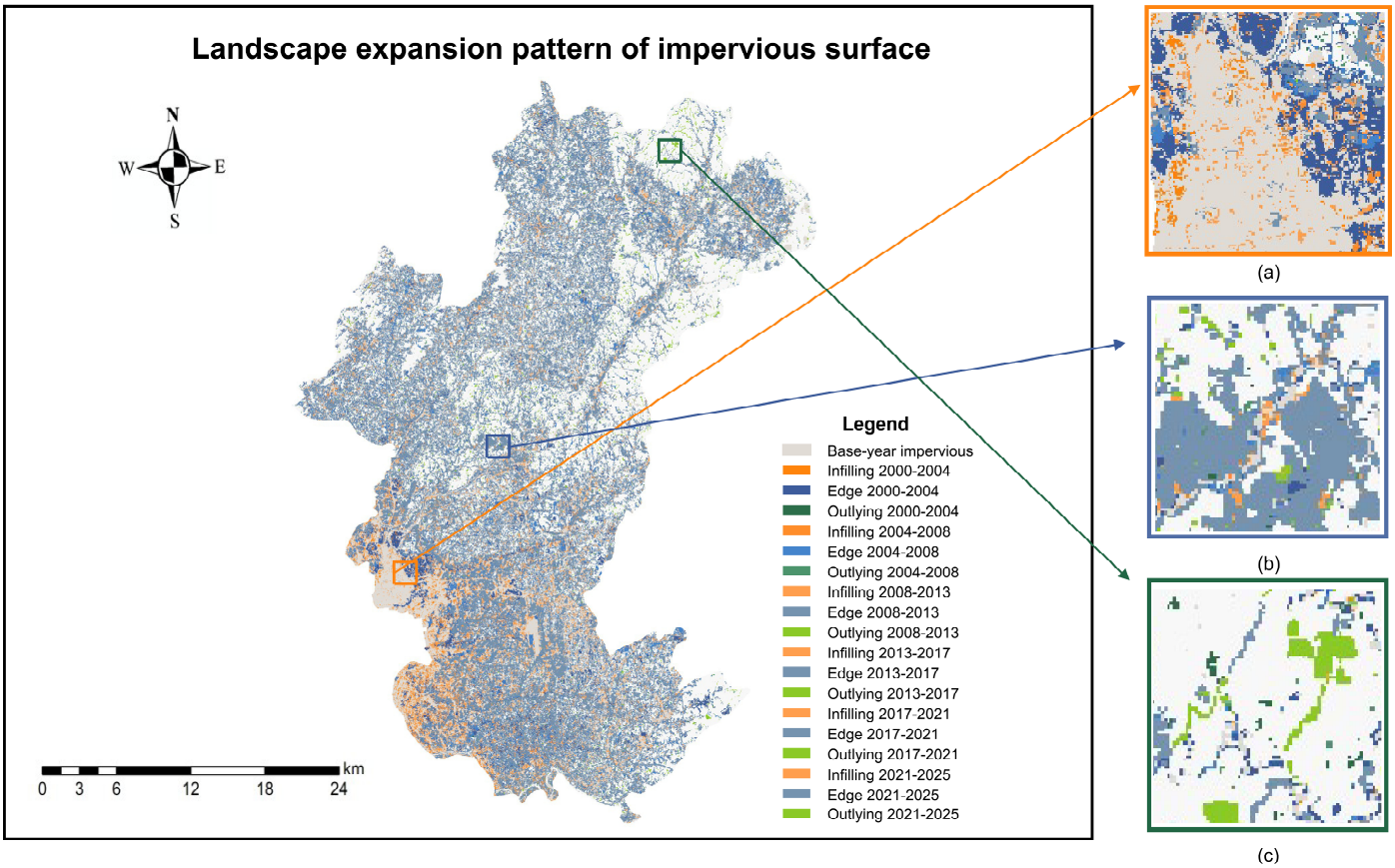


Figure 11. Landscape expansion typologies of impervious surface in Changsha County, 2000–2025. The main map displays the cumulative spatial distribution of three expansion types classified by the Landscape Expansion Index (LEI), with a temporal color gradient. Insets (**a**–**c**) present 3 km × 3 km case studies at locations selected to illustrate the morphological characteristics that support the county's overall urbanization trajectory: (**a**) internal infilling near the county government in the central urban core; (**b**) edge and outlying expansion near the Guoyuan–Ansha town boundary; (**c**) outlying expansion in the northernmost part of Jinjing Town.

Although all three expansion types coexisted throughout the study period, their relative importance and spatial dominance varied across time windows and subregions, providing spatially explicit detail that complements the aggregate trends identified by EII and centroid analyses.

To examine sub-regional differences in expansion patterns, the representative sub-regions of Xingsha and Langli subdistricts, and Huangxing, Jinjing, Jiangbei and Huanghua towns were selected to statistically analyze the expansion patterns of urban and non-urban areas across three time periods (Figure 12). Following the 2000–2010 period, the area of edge expansion pattern in the core subdistricts (Xingsha, Langli) declined significantly, and the built-up area approached saturation. Infilling increased in the later period and approached edge expansion in 2020–2025, while overall expansion intensity in the core stabilized. Together with Figure 11, this indicates a gradual shift from outward sprawl toward internal infill in the central area, consistent with tighter land constraints in mature built-up zones. Among the suburban towns, Huangxing and Huanghua exhibited distinct differences in the expansion patterns. Due to the presence of the Huanghua airport, the urban area of Huanghua maintained relatively high levels of both edge expansion and

infill across all three periods, whilst the expansion of its non-urban areas showed a gradual decline. Although the magnitude of this decline was modest, it nevertheless revealed a gradual weakening of expansion momentum in the suburban rural areas. In Huangxing, the expansion trends and scale of both urban and non-urban areas were relatively similar, demonstrating significant characteristics of urban-rural integration. Within the urban area, infilling remained stable during the first two periods while edge expansion gradually decreased, presenting a co-existence of infill and outward expansion. Jiangbei, though a near-suburban area, falls outside the official urban boundaries of Changsha County. Consequently, its expansion pattern differed somewhat from that of the far-suburban Jinjing. In Zone Jinjing, the total expansion and the outlying increased gradually across the three periods, with the edge pattern remaining dominant throughout, whilst the infilling rebounded in the third period. In Jiangbei, total expansion declined gradually, with the edge expansion decreasing slowly and the infilling remaining largely stable. These regional differences are consistent with the spatial shift of expansion focus from the center to the far-suburban areas.

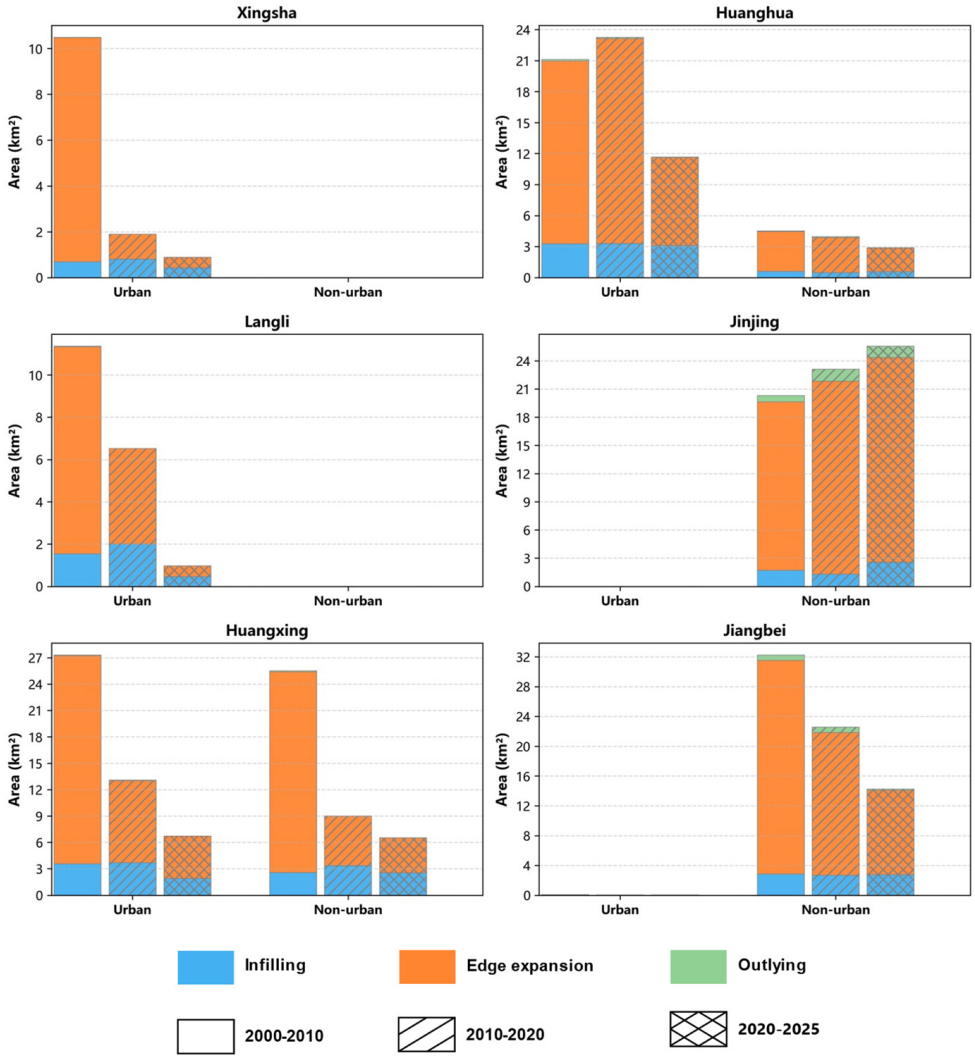


Figure 12. Impervious surface landscape expansion type area statistics for six representative towns (Xingsha, Langli, Huanghua, Huangxing, Jiangbei, and Jinjing) in the study area, 2000–2025: urban and non-urban area comparisons across three key study periods (2000–2010, 2010–2020, 2020–2025).

3.4. Centroid Migration and Density Evolution

The trajectory of the impervious surface centroid was calculated for three primary time periods (Figure 13). The centroid location between 2000 and 2010 reflects the early phase of intensive expansion in the south-central regions of counties such as Huangxing and Xingsha. Between 2010 and 2020, the centroid shifted further south-west by approximately 0.98 km, whilst expansion in the southern core area slowed, corresponding to the spatial layout of new growth hotspots shifting towards Huanghua and the northern periphery. Between 2020 and 2025, the centroid remained largely stable, shifting only about 6 m westward. This reflects the later phase of expansion, where the northern periphery (Jinjing, Kaihui) emerged as new hotspots. However, the scale of this expansion was relatively small, and the total impervious surface area in the northern region remained less than that in the central and southern parts of the county. Overall, the direction of centroid movement closely aligns with the geographic positions of the major new expansion hotspots in each period.

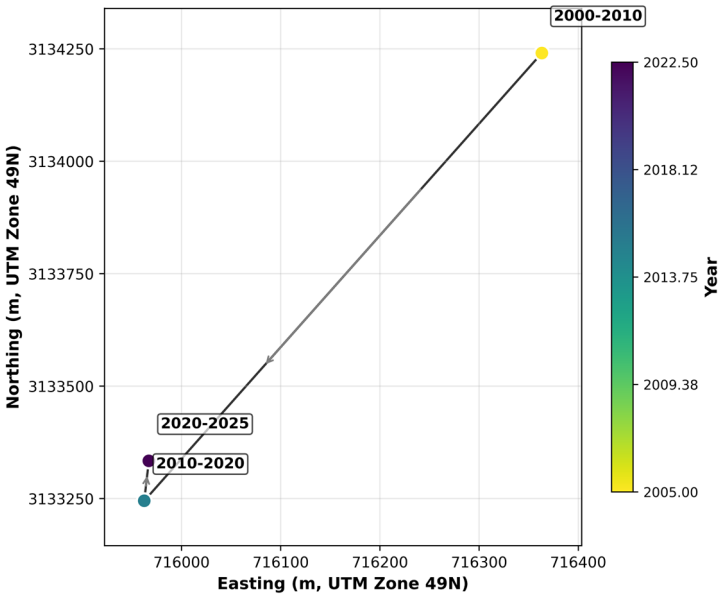


Figure 13. Centroid migration trajectory of impervious surfaces in Changsha County (2000–2010–2020–2025).

The kernel density estimation (KDE) for the three time periods illustrates the spatiotemporal evolution of expansion hotspots (Figure 14). Between 2000 and 2010, high-density areas showed a clear north–south disparity, with higher densities in the south, with the highest kernel density reaching approximately 108. In the south, the Huangxing–Langli area served as the core high-density zone, whilst in the north, the Ansha–Beishan area formed a secondary high-density zone. The southern core area was the principal driver of urbanization during this period. Between 2010 and 2020, the expansion pattern underwent significant changes. The southern high-density zone contracted and shifted eastwards towards Huanghua Town, while the northern zone extended towards Jinjing. The maximum density decreased to 75.4, but the spatial extent of medium- and high-density areas increased relative to the previous period. From 2020 to 2025, the high-density zone shifted further north, with a continuous high-density belt emerging in the northern Jinjing–Kaihui area, where the maximum density decreased to 45.7. Density in the southern core area declined. Overall, the spatial concentration of new expansion decreased in each phase. The high-density zones underwent a spatial transition from being dominated by the southern core, to concurrent development in both the north and south, and finally to being

dominated by the northern periphery, with the center of concentration continuing to shift northwards.

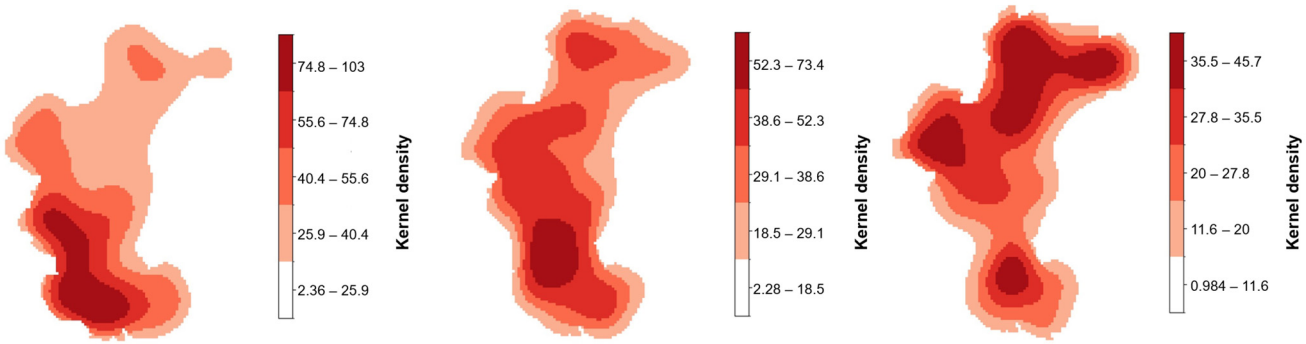


Figure 14. Kernel density estimation (KDE) of newly expanded impervious surfaces in the study area, 2000–2025: three key study periods arranged from left to right (2000–2010, 2010–2020, and 2020–2025).

3.5. Analysis of Driving Factors

Regression analysis at the county scale reveals a strong correlation (correlation coefficient > 0.9) between GDP and registered population (Supplementary Table S9). The multivariate logarithmic model yielded an R^2 of only 0.145. In contrast, the univariate models for GDP and population had R^2 values of 0.085 and 0.017, respectively. These results suggest that aggregate county-level socioeconomic indicators alone are insufficient to explain the spatial variation in impervious surfaces. This underscores the need to incorporate grid-scale geographical drivers for in-depth analysis.

Consequently, linear and logistic regressions were applied at the 1200-m grid scale (Supplementary Table S10). The R^2 of the linear regression (modeling the increase in impervious surface area) decreased from 0.269 for the period 2000–2010 to 0.076 for 2010–2020 and 0.079 for 2020–2025. However, the AUC of the logistic regression consistently remained above 0.81. The ability of geographical drivers to discriminate locations of new expansion remained stable. While geographical factors are associated with expansion locations, their predictive power regarding the extent of expansion weakens as the urbanization process advances.

From the coefficient relationships (Table 2), early expansion in Changsha County was concentrated in relatively flat areas, whilst later new expansion showed a tendency to occur on gentler slopes. The slope coefficient shifted from a significantly negative value in 2000–2020 to a significantly positive value in 2020–2025, whilst the distance from the county center coefficient also shifted from negative to positive (from −0.005 to +0.002), indicating a trend of suburbanization where the focus of expansion moved from the county core to the periphery. Across all three periods, the distance-to-road coefficient remained negative, indicating that new impervious expansion was consistently more likely nearer the road network.

Table 2. Grid-level regression results for impervious surface expansion drivers.

Period	OLS R^2	Slope (β)	Dist_Road (β)	Dist_Center (β)	Logistic_AUC
2000–2010	0.269	−3.079 *	−0.054 ***	−0.005 ***	0.922
2010–2020	0.076	−3.452 ***	−0.025 ***	−0.001 **	0.813
2020–2025	0.079	+1.970 *	−0.025 ***	+0.002 ***	0.841

Note: N = 1269 grid cells (1200 m × 1200 m) per period. OLS, dependent variable: new impervious pixel count; Logistic, dependent variable: expansion occurrence (binary). *** $p < 0.001$, ** $p < 0.01$, * $p < 0.05$.

Panel logistic regression further confirmed the statistical significance of temporal changes in these driver effects (Table 3). The significantly negative interaction term for

slope in 2010–2020 indicates that the negative constraint of slope was weaker than in the baseline period (2000–2010). The interaction term for distance to the county center in the third period was highly significant ($p < 0.001$). The positive effect of distance from the center in the third period differed significantly from that in the base years, reflecting a shift in Changsha County's development towards suburbanization. Meanwhile, none of the interaction terms for distance to roads were statistically significant, further suggesting that the spatial association between road proximity and impervious expansion remained relatively stable across the study periods. Because the road layer was derived from a static OSM network, this association should be interpreted as an accessibility-related spatial relationship rather than direct evidence that road construction causally drove expansion in each period.

Table 3. Panel logit regression with period interaction terms.

Variable	Coefficient	Std. Error	z	*p*-Value	95%CI	Sig
Intercept	3.134	1.087	2.884	0.004	[1.004, 5.263]	**
Slope (deg)	1.215	0.314	3.872	<0.001	[0.600, 1.829]	***
Distance to road (m)	−0.0004	—	−1.779	0.075	[−0.001, 0.000]	#
Distance to center (m)	−0.0001	2.37×10^{-5}	−4.293	<0.001	[−0.000, −0.0001]	***
Period 2010–2020	0.931	1.426	0.653	0.514	[−1.864, 3.727]	
Period 2020–2025	−2.428	1.257	−1.931	0.053	[−4.891, 0.036]	#
Slope × Period 2010–2020	−0.725	0.369	−1.967	0.049	[−1.448, −0.003]	*
Slope × Period 2020–2025	−0.511	0.366	−1.398	0.162	[−1.228, 0.205]	
Dist_road × Period 2010–2020	0.0005	—	1.241	0.215	[−0.000, 0.001]	
Dist_road × Period 2020–2025	−0.000	—	−0.056	0.956	[−0.001, 0.001]	
Dist_center × Period 2010–2020	0.000	3.51×10^{-5}	1.090	0.276	[−0.000, 0.000]	
Dist_center × Period 2020–2025	0.0001	3.39×10^{-5}	3.737	<0.001	[0.0001, 0.000]	***

Note: Model: Logit; N = 3807 (3 periods × 1269 cells); Pseudo $R^2 = 0.242$; LLR *p*-value = 7.15×10^{-22} Base period: 2000–2010. *** $p < 0.001$, ** $p < 0.01$, * $p < 0.05$, # $p < 0.1$.

3.6. Sensitivity Analysis Results

Grid-scale sensitivity analysis for 2020–2025 showed that as the grid size increased from 200 to 2000 m, linear R^2 rose from 0.0226 to 0.1076, whereas the number of grid cells decreased sharply from 40,127 to 466 (Supplementary Table S10). Coarser aggregation therefore reduced local noise and increased apparent explanatory power, but at the cost of fewer observations and reduced representation of within-county heterogeneity. At 1200 m, R^2 (0.0793) and AUC (0.8411) both exceeded those at finer scales (200–1000 m), while retaining 1269 grid cells—approximately 2.7 times the sample size at 2000 m. Although the 2000 m scale yielded the highest R^2 and AUC, only 466 grids remained and more than 99% were classified as experiencing expansion, leading to unstable coefficient directions in the logistic model and indicating over-aggregation. Accordingly, 2000 m was not adopted as the analytical scale. Considering explanatory power, discriminatory performance, sample size, coefficient stability, and spatial granularity, 1200 m was selected as a compromise scale for the driving-factor analysis.

The regression results for the extended later-period sensitivity analysis (2013–2025) yielded a linear R^2 of 0.079 and a logistic AUC of 0.794 (Supplementary Table S11), which were close to the corresponding values for 2020–2025 ($R^2 = 0.079$, AUC = 0.841, Supplementary Table S11). In addition, the coefficient signs of slope, distance to roads, and distance to the county center were consistent between the 2013–2025 and 2020–2025 models. This

suggests that the later-stage driving-factor relationships identified for 2020–2025 were not simply the result of a short five-year window, but remained evident when the analysis was extended to a longer post-2013 period. Together, the sensitivity analyses support the robustness of the interpretations in Section 3.5: recent impervious-surface expansion shifted toward peripheral locations and moderate-slope terrain, while road proximity remained a stable locational factor.

4. Discussion

4.1. Methodological Considerations

Beyond the regional expansion results, several methodological choices merit emphasis from a remote sensing perspective, as they bear directly on the reliability and comparability of the 2000–2025 impervious-surface series. All Landsat data were processed as Level-2 surface reflectance with a uniform 0.3 reflectance cap and identical compositing and clipping thresholds across sensors. Fixed top-10 feature sets and sensor-based grouping (Sections 2.4 and 2.5) prioritized temporal consistency over year-specific maximum accuracy—a requirement often underemphasized in multi-temporal Landsat studies—while maintaining acceptable classification performance.

Uncertainty propagation linked classification accuracy to area-change estimates (Section 2.6.1), supporting a more rigorous interpretation of short-term fluctuations than qualitative assessment alone. Three primary periods (2000–2010, 2010–2020, and 2020–2025) were complemented by annual and four-year analyses (Section 2.2); together with EII, LEI, expansion-rate mapping, centroid shift, and KDE, this framework balanced long-term trends and spatial detail, with Landsat 7 gap-filled versus observed comparisons providing additional checks (Section 3.1). Grid-scale geographical models and qualitative policy assessment (Sections 2.7 and 4.3) addressed both where and how much expansion occurred. These pragmatic remote sensing adaptations are not presented as methodological innovations (Section 2.9) but may inform similar county-scale, multi-sensor time-series studies.

4.2. Urban Expansion Mechanism

The expansion rate in Changsha County declined stepwise over 2000–2025 (Section 3.2), indicating phased deceleration of impervious-area growth at the county scale. County-wide, edge expansion remained the dominant LEI type in all three primary periods (approximately 81–89% of the three-type area), although the infilling share increased (approximately 8–16%) and outlying expansion remained minor (Section 3.3). These proportions summarize compositional change for the county as a whole and do not specify where each type occurred. In the core subdistricts (Xingsha and Langli), the area of edge expansion declined markedly after 2000–2010, and infilling increased as the central built-up area approached saturation (Figure 12). This sub-regional pattern is consistent with internal intensification within the existing core fabric, not with a county-wide shift in total expansion magnitude alone. Li et al. reported that impervious-surface growth in Changsha between 1995 and 2015 combined linear extension of new built-up areas with internal infill [33]; building on this work, the present study refines the analysis to the county scale and reveals differences in infill between near- and far-suburban areas.

Expansion direction shifted from centripetal agglomeration toward suburbanization. Early growth was concentrated around the county-town core, whereas later hotspots moved toward peripheral towns such as Jinjing and Kaihui, where the largest new impervious areas occurred in 2020–2025 (Sections 3.2 and 3.4). The distance-to-county-center coefficient changed from significantly negative (2000–2010) to significantly positive (2020–2025) (Table 2), consistent with new expansion becoming more associated with peripheral loca-

tions in the later period. This directional change is supported independently of the core infilling trend in the previous paragraph: suburbanization cannot be inferred from reduced edge expansion in the core subdistricts alone. Scattered infill in the central built-up area (Figure 11) coexisted with—not as a substitute for—these peripheral hotspots. Compared with concentric expansion in Chuzhou [34], multi-core development in Nanjing [8,14], and continuous sprawl in the Pearl River Delta [7], the spatial trajectory of Changsha County reflects distinctive county-level urbanization in a hilly setting, combining later peripheral extension with ongoing internal intensification in the core.

4.3. Driving Factor Analysis

The expansion pattern of Changsha County does not follow a common model but was shaped by the interplay of topography and policy. Understanding the shift in driving mechanisms is another key to comprehending its expansion trajectory. Geographical constraints have undergone a phased evolution, with the slope coefficient shifting from negative to positive, revealing the dynamic relationship between terrain and urban expansion during urban expansion. Early expansion was concentrated in flatter areas with gentler slopes, aligning with the typical urbanization pattern of initially prioritizing easily developable areas. Studies on the layout of rural settlements in Changsha County have also shown that they are significantly influenced by slope [35], whilst hilly terrain accounts for approximately 89.6% of the county [36]. And coupled with rapid development in earlier decades, this meant that flat land within the county was largely depleted. This restricted the leapfrog (outlying) development, directing subsequent expansion toward edge growth, with remaining developable plots naturally extending into gently sloping hills. Research on Changsha County indicates that the Enhanced Vegetation Index (EVI) in Changsha County declined rapidly, and vegetation changes slowed after the core area was developed [37]. This pattern indirectly supports the trend of shifting towards sloping terrain in later stages. In the panel model, the interaction term between slope and the second period was significantly negative, statistically confirming that the constraining effect of slope significantly weakened over the study timeline. Collectively, these findings indicate that the influence of geographical factors is stronger in the early stages of urbanization and tends to weaken in later stages. Separately, later-stage shifts in expansion mode in the central urban area similarly reflect the post-2020 strategic emphasis on compact growth and intensification. Local governments have turned to internal land consolidation and, through planning controls, to optimizing development intensity and spatial form rather than continued outward sprawl in the urban core.

The continuous decline in the R^2 of the linear model's explanatory power for new development contrasts with the stable AUC in the logistic regression (Table 2). This contrast reveals a fundamental difference in the role played by geographical drivers at different stages in Changsha County. Early expansion was highly concentrated in prime areas like Xingsha and Huangxing, primarily developing parts of the central urban area. In this phase, geographical conditions offer a relatively high degree of explanation for the extent (magnitude) of expansion. In the latter two periods, however, expansion tends to become fragmented and dispersed, and the extent of new development was increasingly influenced by non-geographical factors such as policy-related land supply and project implementation. The declining R^2 quantifies this transition. Nevertheless, the AUC remained consistently high, indicating that geographical factors retained strong power to distinguish where expansion occurred, even though the extent of expansion is difficult to predict. And new expansion continued to follow discernible geographical patterns: early new development was adjacent to the old urban core, whereas later development was more often adjacent to specific outlying townships. Road proximity remained a consistent accessibility-related

locational factor throughout the study period, although it should not be interpreted as a year-specific causal effect of road construction, given the static OSM road network used in this study. Together, these findings suggest that geographical and accessibility-related conditions shaped the spatial likelihood of expansion, but were not sufficient to explain the magnitude and timing of development in Changsha County. In later stages, the spatial pattern was shaped by the interplay of policy and specific locational advantages. Consequently, urban expansion in Changsha County transitioned from a phase of extensive, contiguous development to one characterized by more intensive infill.

Yu Si et al. identified that the central and southern parts of Changsha County were expansion hotspots during 2010–2020, noting an increase in semi-urban areas under combined socio-economic and policy influences [38]. This finding is consistent with a growing policy-related component alongside geographical factors in that period. Sustained edge expansion in peri-urban areas during the same period (Figure 11) aligns spatially with the Changsha metropolitan area's multi-node spatial layout ("one new city and three major towns") and with platform-oriented development such as the aerotropolis and Huangxing exhibition zones; this relationship is discussed as spatial correspondence rather than as a quantitatively tested causal effect. By contrast, scattered outlying expansion around Jinjing in the northern periphery is consistent with rural revitalization, ecological transition, and agro-tourism-oriented policies, supported locally through projects such as rural road improvement ("four good rural roads"), tea-tourism integration, and rural tourism. The new, scattered developments in the outlying townships of Changsha County between 2020 and 2025 differ spatially from the contiguous development in the core area. These patches are more fragmented and often adjacent to existing settlements, a pattern that links to the rural revitalization strategy promoted in recent years. Guoyuan Town exemplifies this pattern. There, a collaborative governance model (government guidance, enterprise leadership and villager participation) and diversified industries facilitated rural settlement renewal and expansion [39]. This type of spot development, driven by rural revitalization, constitutes the primary form of growth in outlying townships. Furthermore, Key policy milestones in Changsha County—including the upgrading of the Economic and Technological Development Zone in 2000, the approval of the Aerotropolis Economic Zone in 2016, and the promotion of high-quality development policies after 2020—closely coincided with the temporal shifts of expansion hotspots identified in this study. This temporal alignment underscores the influential role of policy in driving the observed phased transformations.

4.4. Assessment of Semi-Decadal Change Reliability

The apparent net decreases in impervious-surface area during 2005–2010 and 2015–2020 require cautious interpretation because they occur at semi-decadal scales and coincide with periods affected by Landsat 7 SLC-off gap filling. This study does not attribute these fluctuations simply to real land-cover change or to processing error alone. Instead, they are evaluated using two complementary lines of evidence: (1) uncertainty propagation of mapped area changes and (2) a dedicated comparison of Landsat 7 gap-filled versus originally observed pixels.

Uncertainty propagation indicates that both semi-decadal negative changes fall within the propagated classification-uncertainty range, whereas the net increases for the primary periods 2000–2010 and 2010–2020 exceed this range (Supplementary Table S3). The semi-decadal negative values are therefore not statistically sufficient to support county-scale de-urbanization. By contrast, decadal-scale growth signals can be distinguished from classification uncertainty, supporting the main conclusions on long-term impervious-surface expansion.

The gap-filled versus originally observed pixel comparison provides further context for these fluctuations (Section 3.1; Supplementary Table S4). In two representative Landsat 7 years, impervious proportions were consistently higher in gap-filled than in originally observed areas, indicating a tendency toward local overestimation in filled pixels. When later higher-quality observations reduce such overestimation, the time series may show apparent "loss" even without widespread real removal of impervious surfaces. The semi-decadal net decreases in Table 1 are therefore better interpreted as data-quality-related fluctuations rather than as robust evidence of real land-cover loss. This interpretation does not negate the value of annual and semi-decadal maps for fine-scale spatial pattern analysis; it clarifies their scope—such maps are suited to detailed spatial interpretation, whereas main quantitative conclusions should rely on the primary periods and be supported by uncertainty assessment.

4.5. Limitations

Although Section 4.4 indicates that semi-decadal apparent decreases are more consistent with data-quality fluctuations than with county-scale de-urbanization, several limitations remain. Landsat 7 SLC-off gap filling is an inherent constraint of the historical Landsat record and cannot be fully removed retrospectively. Validation samples falling within gap-filled pixels are limited; sample-based accuracy comparisons should therefore be treated as supporting diagnostic evidence rather than as final independent accuracy estimates for those areas. Reliance on Landsat classification alone likewise cannot fully exclude localized real land-cover changes, including small-scale demolition, re-greening, or water-body adjustment. Future work should combine field validation or high-resolution imagery cross-checks to further test interpretations of short-term apparent losses.

At 30 m Landsat resolution, bare soil and impervious surfaces can be spectrally similar, which inevitably causes some classification errors [40–42], whereas some impervious surfaces may be omitted or classified as bare soil because of their spectral properties [43]. Such confusion is typically bidirectional and spatially variable at medium resolution and can reduce overall accuracy if strongly systematic [44]. In this study, however, mean validation metrics (OA = 91.44%, Kappa = 0.8394, F1 = 0.9150; Supplementary Table S1) suggest that this confusion did not substantially undermine overall classifier reliability or systematically bias long-term expansion trends. Future studies could use multi-source fusion (e.g., Sentinel-1 SAR, night-time lights, and DEM) to further reduce bare-soil/impervious commission errors [45].

The OSM road network used here is static and cannot fully represent road evolution between 2000 and 2025. The distance-to-road variable should therefore be interpreted as a spatial proxy for accessibility and proximity to transport corridors, not as a period-specific causal effect of road construction; co-evolution or reverse causality may still exist. Historical road maps, transportation records, planning documents, or multi-temporal road networks from high-resolution imagery could help separate antecedent and concurrent road effects in future work.

In the panel logistic model, approximately 22% of observations were perfectly predicted, which may inflate the variance of coefficient estimates. Although the model converged and key interaction terms were significant, the magnitudes of coefficients should be interpreted cautiously. Finally, although the analysis describes a shift from stronger topographic constraints toward socioeconomic and policy-related influences, policy effects were assessed qualitatively through spatiotemporal correspondence between policy milestones and expansion hotspots, not through explicit quantitative policy variables. Future research could quantify policy contributions using planning documents, land-transaction data, or digitised historical development-zone boundaries as additional predictors.

5. Conclusions

Based on a Landsat time series for Changsha County (2000–2025), this study developed a multi-dimensional framework integrating area change, expansion intensity, expansion rate, centroid shift, kernel density estimation, and driving-factor analysis to characterize county-scale urban expansion. Impervious-surface area increased throughout the 25-year period, but expansion showed clear phased deceleration: rapid growth in 2000–2010 (net increase of 177.9 km^2), slower growth in 2010–2020 (77.98 km^2), and further slowdown in 2020–2025 (21.64 km^2). Edge expansion remained dominant (approximately 80% of the three LEI types), while infilling increased in later stages, indicating more compact development alongside continued outward growth. Geographical drivers changed over time: slope and distance to the county center constrained early expansion but weakened later, whereas road proximity showed a stable spatial association with new expansion as an accessibility-related locational factor rather than a direct historical causal effect of road construction. In later stages, as readily developable plain land became increasingly scarce, policy-related factors—such as new economic zones and rural revitalization programs—became important contextual influences on decentralized growth in suburban and outlying townships.

Long-term time-series studies of urban expansion continue to rely on Landsat, yet cloud cover in humid subtropical regions and Landsat 7 SLC-off gap filling can add uncertainty to temporal analyses. This study addressed these issues through gap-filled versus originally observed pixel comparisons, uncertainty propagation of mapped area changes, and sensitivity analyses of grid scale and analysis period, thereby supporting more cautious interpretation of short-term fluctuations and the primary-period expansion trends.

This work clarifies urbanization pathways in a representative county of central China and provides a scientific basis for differentiated land-use planning and sustainable urban management. Beyond Changsha County, the framework is transferable to other rapidly urbanizing counties with similar multi-sensor, long-term data needs—for example, delineating urban growth boundaries, monitoring spatial planning implementation, or assessing land-cover effects of rural revitalization policies. The combination of sensor-family fixed feature sets, reference-year sample migration, and quantitative uncertainty propagation offers a practical approach for consistent long-term impervious-surface mapping elsewhere.

Supplementary Materials: The following supporting information can be downloaded at: https://www.mdpi.com/article/10.3390/rs18152555/s1, Table S1. Annual sample sizes, class distribution, and classification accuracy metrics for each reference year; Table S2: Grouping of Landsat imagery and selection of baseline years for classification; Table S3. Area-change uncertainty propagation based on classification accuracy metrics; Table S4. Comparison of impervious-surface pixel proportions and sample-based classification accuracy between gap-filled and originally observed regions for two representative Landsat 7 years; Table S5: Annual percentage of impervious surface area in Changsha County, 2000–2025; Table S6: Three-Period Summary (Based on Direct Area Difference); Table S7: Expansion characteristics of impervious surfaces across three periods; Table S8: Landscape expansion pattern statistics by period; Table S9: County-level regression results for impervious area vs. socioeconomic factors (2000–2025); Table S10: Sensitivity analysis: grid-scale effects on model performance (2020–2025); Table S11: Sensitivity analysis: comparison of regression results between longer period subset and main study period; Figure S1. Confusion matrices for all 16 reference years, showing per-class user's accuracy and producer's accuracy for impervious and pervious surfaces.

Author Contributions: Conceptualization, Y.C. and L.Z.; methodology, Y.C.; validation, Y.C.; formal analysis, Y.C.; investigation, Y.C.; resources, Y.C.; data curation, Y.C., Z.W. and X.Y.; writing—original draft preparation, Y.C.; writing—review and editing, Y.C. and L.Z.; supervision, L.Z., Y.L., Q.X. and Q.Z.; project administration, Y.C. and L.Z.; funding acquisition, Y.C. and L.Z. All authors have read and agreed to the published version of the manuscript.

Funding: This research was funded by the Open Fund of Engineering Laboratory of Spatial Information Technology of Highway Geological Disaster Early Warning in Hunan Province (Changsha University of Science & Technology), grant number kfj230703; the Hunan Provincial Natural Science Foundation Youth Fund Project Category C, grant number 2025JJ60235; and the Scientific Research Foundation of Hunan Education Department, grant number 24C0142.

Data Availability Statement: The data and code that support the findings of this study are available from the corresponding author upon reasonable request.

Acknowledgments: The authors would like to thank the anonymous reviewers for their constructive comments, which greatly helped to improve the quality of this manuscript. The authors also sincerely thank Lihong Zhu for her invaluable guidance and support throughout this research.

Conflicts of Interest: The authors declare no conflicts of interest.

References

1. Bai, X.; Chen, J.; Shi, P. Landscape Urbanization and Economic Growth in China: Positive Feedbacks and Sustainability Dilemmas. *Environ. Sci. Technol.* **2012**, *46*, 132–139. [CrossRef] [PubMed]
2. Liu, Z.H.; Li, Y.; Peng, J. Research Progress on Water Environmental Effects of Urban Impervious Surface. *Prog. Geogr.* **2011**, *30*, 275–281.
3. Lin, Y.S.; Xu, H.Q.; Zhou, R. Study on Urban Impervious Surface and Its Relationship with Urban Heat Island: A Case Study of Quanzhou City. *Remote Sens. Technol. Appl.* **2007**, *22*, 14–19.
4. Wang, L.L.; Zhang, X.Y. Spatiotemporal Evolution of Impervious Surface in the Yellow River Water Receiving Area of Henan Province Based on Google Earth Engine. *Yellow River* **2022**, *44*, 76–80, 86. [CrossRef]
5. Kuang, K.X.; Yang, Y.B.; Gao, Y.N.; Liu, Y.X. A Random Forest Extraction Method for Impervious Surfaces by Synergizing Sentinel SAR and Optical Image Multi-Features. *Remote Sens. Technol. Appl.* **2023**, *38*, 422–431.
6. Yin, R.Y. Research on Methods for Mining Large-Scale and Long-Term Impervious Surface Coverage and Change Information. Ph.D. Thesis, University of Chinese Academy of Sciences (Aerospace Information Research Institute, Chinese Academy of Sciences), Beijing, China, 2022.
7. Kong, D.W. Extraction and Spatiotemporal Characteristics Analysis of Impervious Layers Based on Long-Term Satellite Remote Sensing: A Case Study of the Pearl River Delta Region in Guangdong Province. *Geomat. Spat. Inf. Technol.* **2025**, *48*, 146–149.
8. Wang, S.S.; Pu, Y.X.; Li, S.F.; Li, R.J.; Li, M.H. Exploring Urban Growth Patterns Using Long-Term Watershed Impervious Surface Datasets: A Case Study of the Qinhuai River Basin. *Remote Sens. Technol. Appl.* **2022**, *37*, 739–750. [CrossRef]
9. Gao, M.-N.; Hu, Y.-X.; Shang, G.-F.; Li, W. Research on the Impact of Spatial and Temporal Changes in Ecological Product Value in Hebei Province Based on Land Use Changes. *Sci. Rep.* **2025**, *15*, 9571. [CrossRef] [PubMed]
10. Chen, X.; Wu, S.; Wu, J. Characteristics and Formation Mechanism of Land Use Conflicts in Northern Anhui: A Case Study of Funan County. *Heliyon* **2024**, *10*, e22923. [CrossRef] [PubMed]
11. Fan, L.; Zhang, B.; Wang, Y.; Zhao, W.; Dong, S. Analysis on Process of Temporal and Spatial Evolution of Urban Built-up Area Expansion in the Yellow River Basin. *PLoS ONE* **2022**, *17*, e0270370. [CrossRef] [PubMed]
12. Sharma, M.; Abhay, R.K. Urban Growth and Quality of Life: Inter-District and Intra-District Analysis of Housing in NCT-Delhi, 2001–2011–2020. *GeoJournal* **2022**, *87*, 797–819. [CrossRef] [PubMed]
13. Liu, S.; Xia, Y.; Ji, Y.; Lai, W.; Li, J.; Yin, Y.; Qi, J.; Chang, Y.; Sun, H. Balancing Urban Expansion and Ecological Connectivity through Ecological Network Optimization—A Case Study of ChangSha County. *Land* **2023**, *12*, 1379. [CrossRef]
14. Qian, Z.Y.; Fu, H.Y.; Wang, Y.; Zhang, Y.T. Characteristics of Urban Expansion and Morphological Evolution in Nanjing from 2004 to 2016. *Remote Sens. Land Resour.* **2019**, *31*, 149–156.
15. Zhang, A.Q.; Xia, C.; Lin, J.; Chu, J.Q. Landscape Evolution Characteristic Index and Its Application. *Prog. Geogr.* **2018**, *37*, 811–822.
16. He, Q.S.; Wang, M.J.; Cai, R.Z.M. Research on Urban Compactness Analysis Based on Multi-Dimensional Landscape Expansion Index. *Geomat. World* **2021**, *28*, 58–65.
17. Gao, B.P. Study on Urban Expansion and Its Ecological Environment Effects in Central Yunnan Urban Agglomeration. Ph.D. Thesis, Yunnan Normal University, Kunming, China, 2023.
18. Weng, Q. Remote Sensing of Impervious Surfaces in the Urban Areas: Requirements, Methods, and Trends. *Remote Sens. Environ.* **2012**, *117*, 34–49. [CrossRef]
19. Tang, X.; Qu, W.; Zhang, J.; Li, G.; Zhang, X.; Yang, S.; Song, X.; Zhao, M.; Han, R. Driving Mechanism of Urban Expansion in the Bohai Rim Urban Agglomeration from the Perspective of Spatiotemporal Dynamic Analysis. *Sci. Rep.* **2024**, *14*, 31191. [CrossRef] [PubMed]

20. Zhang, L.; Weng, Q. Annual Dynamics of Impervious Surface in the Pearl River Delta, China, from 1988 to 2013, Using Time Series Landsat Imagery. *ISPRS J. Photogramm. Remote Sens.* **2016**, *113*, 86–96. [CrossRef]
21. Seto, K.C.; Fragkias, M. Quantifying Spatiotemporal Patterns of Urban Land-Use Change in Four Cities of China with Time Series Landscape Metrics. *Landsc. Ecol.* **2005**, *20*, 871–888. [CrossRef]
22. Sun, L.N.; Li, K. Research on the Evolution of Urban Form and Development Direction in Weifang Based on Centroid Migration. *China Hous. Facil.* **2023**, 13–15.
23. Liao, J.J.; Li, X.; Wang, Z.Y.; Zhang, K.; Lyu, J.T. Study on the Growth Pattern and Driving Factors of Construction Land in Chang-Zhu-Tan Metropolitan Area. *World Reg. Stud.* **2023**, *32*, 133–145.
24. Shi, W.; Tian, J.; Namaiti, A.; Xing, X. Spatial-Temporal Evolution and Driving Factors of the Coupling Coordination between Urbanization and Urban Resilience: A Case Study of the 167 Counties in Hebei Province. *Int. J. Environ. Res. Public Health* **2022**, *19*, 13128. [CrossRef] [PubMed]
25. Ou, C.; Tan, X.L. Comprehensive Measurement and Regional Type Division of Rural Hollowing in Rapid Urbanization Areas: A Case Study of Chang-Zhu-Tan Area. *Hubei Agric. Sci.* **2016**, *55*, 2695–2700. [CrossRef]
26. Kennedy, R.E.; Cohen, W.B.; Schroeder, T.A. Trajectory-Based Change Detection for Automated Characterization of Forest Disturbance Dynamics. *Remote Sens. Environ.* **2007**, *110*, 370–386. [CrossRef]
27. Wu, W.; Sun, X.; Wang, X.; Fan, J.; Luo, J.; Shen, Y.; Yang, Y. A Long Time-Series Radiometric Normalization Method for Landsat Images. *Sensors* **2018**, *18*, 4505. [CrossRef] [PubMed]
28. Vermote, E.; Roger, J.C.; Franch, B.; Skakun, S. LaSRC (Land Surface Reflectance Code): Overview, Application and Validation Using MODIS, VIIRS, LANDSAT and Sentinel 2 Data's. In *Proceedings of the IGARSS 2018–2018 IEEE International Geoscience and Remote Sensing Symposium*; IEEE: Valencia, Spain, 2018; pp. 8173–8176.
29. Guo, X.; Zhang, C.; Luo, W.; Yang, J.; Yang, M. Urban Impervious Surface Extraction Based on Multi-Features and Random Forest. *IEEE Access* **2020**, *8*, 226609–226623. [CrossRef]
30. Kumar, S.; Varshney, S.; Jain, U.; Johri, P.; Almazyad, A.S.; Mohamed, A.W.; Hosseinzadeh, M.; Shokouhifar, M. EODA: A Three-Stage Efficient Outlier Detection Approach Using Boruta-RF Feature Selection and Enhanced KNN-Based Clustering Algorithm. *PLoS ONE* **2025**, *20*, e0322738. [CrossRef] [PubMed]
31. Liu, X.; Li, X.; Chen, Y.; Tan, Z.; Li, S.; Ai, B. A New Landscape Index for Quantifying Urban Expansion Using Multi-Temporal Remotely Sensed Data. *Landsc. Ecol.* **2010**, *25*, 671–682. [CrossRef]
32. Tian, Y.; Shuai, Y.; Ma, X.; Shao, C.; Liu, T.; Tuerhanjiang, L. Improved Landscape Expansion Index and Its Application to Urban Growth in Urumqi. *Remote Sens.* **2022**, *14*, 5255. [CrossRef]
33. Li, Z.; Li, P.; Liu, Q. Study on a Model of Water Surface Growth and Its Driving Factors in Large Cities along the Middle Reaches of the Yangtze River. *Acta Ecol. Sin.* **2018**, *38*, 3766–3774. [CrossRef]
34. Cao, J.; Zhang, X.; Song, D.X. Spatiotemporal Change Analysis of Impervious Surface in Chuzhou City Based on Remote Sensing Data. *Anhui Agric. Sci. Bull.* **2026**, *32*, 71–74. [CrossRef]
35. Tan, S. Research on the Layout Optimization of Rural Residential Land in Changsha County. Master's Thesis, Hunan Normal University, Changsha, China, 2016.
36. He, Q.L.; She, D.L.; Chen, W.L.; Zhang, P. Research on Optimization and Control Strategies of Water Surface Ratio in Hilly Small Watersheds: A Case Study of Changsha County. *Water Resour. Prot.* **2026**. *online*.
37. Jiang, S.C. Impact of Urbanization on Vegetation Growth Trends in Changsha City from 2000 to 2017. Master's Thesis, Central South University of Forestry and Technology, Changsha, China, 2021.
38. Yu, S.; Peng, P. Identification and Spatial Evolution Characteristics of Peri-urban Areas in Changsha. *J. Urban Stud.* **2023**, *44*, 10–18.
39. Huang, J.H.; Deng, Y.Q. Interconnection and Common Prosperity: The Construction of Actor Network in the New Endogenous Development of Rural Areas: Based on a Case Analysis of Xunlonghe Village in Changsha County. *J. Jimei Univ. (Philos. Soc. Sci.)* **2026**, *29*, 60–74.
40. Bauer, M.; Loffelholz, B.; Wilson, B. Estimating and Mapping Impervious Surface Area by Regression Analysis of Landsat Imagery. In *Remote Sensing of Impervious Surfaces*; Weng, Q., Ed.; Remote Sensing Applications Series; CRC Press: Boca Raton, FL, USA, 2007; Volume 20073946, ISBN 978-1-4200-4374-7.
41. Hidayati, I.N.; Suharyadi, R. A Comparative Study of Various Indices for Extraction Urban Impervious Surface of Landsat 8 OLI. *For. Geo.* **2019**, *33*, 162–172. [CrossRef]
42. Delaney, B.; Tansey, K.; Whelan, M. Satellite Remote Sensing Techniques and Limitations for Identifying Bare Soil. *Remote Sens.* **2025**, *17*, 630. [CrossRef]
43. Zhang, X.; Liu, L.; Wu, C.; Chen, X.; Gao, Y.; Xie, S.; Zhang, B. Development of a Global 30 m Impervious Surface Map Using Multisource and Multitemporal Remote Sensing Datasets with the Google Earth Engine Platform. *Earth Syst. Sci. Data* **2020**, *12*, 1625–1648. [CrossRef]

44. Lou, Y.X. Two Kinds of Impervious Surface Indices for Restraining Bare Soil. *AAM* **2022**, *11*, 8442–8452. [CrossRef]
45. Zhang, Q. Urban Impervious Surface Extraction Supported by Multi-Source Remote Sensing Data: A Case Study of Tianjin. *Surv. Eng.* **2023**, *32*, 69–75. [CrossRef]

Disclaimer/Publisher's Note: The statements, opinions and data contained in all publications are solely those of the individual author(s) and contributor(s) and not of MDPI and/or the editor(s). MDPI and/or the editor(s) disclaim responsibility for any injury to people or property resulting from any ideas, methods, instructions or products referred to in the content.